AGU ADVANCING EARTH AND SPACE SCIENCES

Earth and Space Science

RESEARCH ARTICLE
10.1029/2025EA004637

Special Collection:
TEMPO Data Products, Science, and Applications

Spectral Calibration for TEMPO (Tropospheric Emissions: Monitoring of Pollution): Algorithm Description and Trending of Spectral Performance

Weizhen Hou[1], Xiong Liu[1], John C. Houck[1], Heesung Chong[1], Christopher Chan Miller[1], David E. Flittner[2], James L. Carr[3], Kelly Chance[1], Huiqun Wang[1], Gonzalo González Abad[1], Caroline R. Nowlan[1], Jun Wang[4], Junsung Park[1], Nischal Mishra[5], John E. Davis[1], Raid M. Suleiman[1], and Jean Fitzmaurice[1]

[1]Atomic and Molecular Physics Division, Center for Astrophysics | Harvard & Smithsonian, Cambridge, MA, USA, [2]NASA Langley Research Center, Hampton, VA, USA, [3]Carr Astronautics, Greenbelt, MD, USA, [4]Department of Chemical and Biochemical Engineering, Iowa Technology Institute, Center for Global and Regional Environmental Research, University of Iowa, Iowa City, IA, USA, [5]Applied Physics Laboratory, Johns Hopkins University, Laurel, MD, USA

Abstract The Tropospheric Emissions: Monitoring of Pollution (TEMPO) instrument provides continuous, high-resolution observations of atmospheric pollutants over North America from geostationary orbit. This study introduces an on-orbit spectral calibration algorithm implemented in the TEMPO Version 3 Level 0–1 processor, covering both operational irradiance and radiance wavelength calibrations and offline slit function retrievals. Irradiance wavelength calibration accuracy was evaluated, with the TSIS-1 hybrid solar reference spectrum chosen due to its low fitting residuals. Accordingly, first- and second-order Chebyshev-polynomial fittings are applied to UV and VIS, respectively, to derive the wavelength grid. Earth-view radiance wavelength calibration updates the wavelength grid based on the latest solar irradiance calibration result by fitting a wavelength shift. To optimize efficiency and accuracy, a narrow spectral window of 100 channels (320–340 nm for UV and 630–650 nm for VIS) was selected, with wavelength shift uncertainties of 0.002 nm (UV) and 0.006 nm (VIS). Radiance calibration results shows that the wavelength shifts of inhomogeneous pixels vary relatively significantly. We perform a 22-month trend analysis of the TEMPO solar irradiance spectral performance. Compared to first light, the wavelength shift gradually increases, reaching 0.08–0.09 nm in July 2024, and then remains stable. The offline slit function parameters, retrieved from several narrow spectral windows using a super-Gaussian function, show minor variations during the 22-month on-obit operation and did not deviate significantly from prelaunch. This study supports the long-term L1b data processing for TEMPO and provides an instrument spectral calibration framework applicable for future geostationary orbit spectrometers.

Plain Language Summary The TEMPO satellite instruments measure air pollution over North America hourly from a fixed-point relative to Earth in geostationary orbit. To ensure accuracy, scientists must carefully calibrate how the instrument captures different wavelengths of light. This paper describes how we calibrated using sunlight as a reference, including both measurements of sunlight and Earth-reflected light by TEMPO. We also conducted long-term monitoring of the instrument's performance. Having operated in orbit for nearly 2 years, the instrument showed only minor, expected changes in wavelength calibration and optical characteristics. Furthermore, we investigated how scene variations, such as cloud cover or different surface types, affected the calibration results. The techniques presented in this paper help maintain data quality throughout TEMPO's operational lifecycle and are expected to benefit other similar future geostationary air pollution monitoring missions.

Key Points:

- On-orbit spectral calibration for TEMPO is implemented and validated for both irradiance and radiance using Chebyshev polynomial fits
- Wavelength shifts remain small and stable over 22 months, slit function parameters show minimal variation from prelaunch values
- A small-window method provides relative accurate, efficient radiance spectral calibration and captures scene inhomogeneity effects

Correspondence to:
W. Hou,
weizhen.hou@cfa.harvard.edu

Citation:
Hou, W., Liu, X., Houck, J. C., Chong, H., Chan Miller, C., Flittner, D. E., et al. (2026). Spectral calibration for TEMPO (tropospheric emissions: Monitoring of pollution): Algorithm description and trending of spectral performance. *Earth and Space Science*, *13*, e2025EA004637. https://doi.org/10.1029/2025EA004637

Received 4 AUG 2025
Accepted 29 DEC 2025

Author Contributions:
Conceptualization: Weizhen Hou, Xiong Liu
Data curation: Xiong Liu, John C. Houck, Heesung Chong, David E. Flittner, James L. Carr, Kelly Chance, Huiqun Wang, Gonzalo González Abad, Caroline R. Nowlan, Nischal Mishra, John E. Davis, Raid M. Suleiman, Jean Fitzmaurice
Formal analysis: Weizhen Hou, John C. Houck, Heesung Chong, Christopher Chan Miller, Huiqun Wang, Junsung Park, Nischal Mishra
Funding acquisition: Xiong Liu, Kelly Chance, Jun Wang
Investigation: Weizhen Hou, Xiong Liu, Jun Wang

1. Introduction

The successful launch of the Tropospheric Emissions: Monitoring of Pollution (TEMPO) instrument aboard the Intelsat 40e (IS-40e) satellite makes a significant advancement in the monitoring of atmospheric trace gases in North America (Wang et al., 2025; Zoogman et al., 2017). TEMPO operates in a Geostationary Earth Orbit at 91°W, continuously observing the same geographic region with high temporal resolution, providing near-real-time data on air quality as represented in nitrogen dioxide (NO_2), ozone (O_3), and other atmospheric constituents.

Methodology: Weizhen Hou, Xiong Liu, Christopher Chan Miller, David E. Flittner, Kelly Chance
Project administration: Xiong Liu, Kelly Chance, Gonzalo González Abad, Caroline R. Nowlan, Raid M. Suleiman
Resources: Xiong Liu, David E. Flittner, James L. Carr, Kelly Chance, Gonzalo González Abad, John E. Davis, Raid M. Suleiman, Jean Fitzmaurice
Software: Xiong Liu, John C. Houck, Heesung Chong, Christopher Chan Miller, David E. Flittner, James L. Carr, Huiqun Wang, Gonzalo González Abad, Junsung Park, John E. Davis
Supervision: Xiong Liu, Kelly Chance
Validation: Weizhen Hou, John C. Houck, Heesung Chong, Christopher Chan Miller, David E. Flittner, James L. Carr, Huiqun Wang, Gonzalo González Abad, Caroline R. Nowlan, Jun Wang, Junsung Park, Nischal Mishra
Visualization: Weizhen Hou, John C. Houck
Writing – original draft: Weizhen Hou
Writing – review & editing: Weizhen Hou, Xiong Liu, John C. Houck, Heesung Chong, Christopher Chan Miller, David E. Flittner, James L. Carr, Kelly Chance, Huiqun Wang, Gonzalo González Abad, Caroline R. Nowlan, Jun Wang, Junsung Park, Nischal Mishra, John E. Davis, Raid M. Suleiman, Jean Fitzmaurice

For atmospheric hyperspectral remote sensing instruments such as TEMPO, accurate spectral calibration is crucial because it directly affects the quality of the Level 1b (L1b) data, and consequently affect the accuracy of trace gases and aerosol properties inversion. Even small spectral calibration uncertainties can lead to significant biases in spectral fitting, affecting the retrieval of key atmospheric components, such as O_3, NO_2, formaldehyde (HCHO), and water vapor (H_2O) (Chan et al., 2020; Chance et al., 2000; Gonzalez Abad et al., 2019; Liu et al., 2007; Nowlan et al., 2016). Accurate determination of the slit function, or instrument spectral response function, is particular important for hyperspectral instruments like TEMPO, because it affects the spectral convolution with a high-resolution molecular reference spectra, thus influencing trace gas inversion (Voors et al., 2006). Inaccuracies in slit function parameterization can cause systematic retrieval errors (Beirle et al., 2013; Sihler et al., 2016).

Because on-orbit spectral alignment and response are affected by a variety of parameters, on-orbit spectral calibration of the wavelength grid and the slit function is necessary. Mechanical stress and vibration during launch can cause slight optical deviations. Simultaneously, thermal changes in orbit can alter focal length and detector alignment, potentially lead to wavelength drifts over time (Sun, Liu, Huang, et al., 2017). Furthermore, scene inhomogeneity (e.g., differences in surface reflectivity, cloud cover, aerosols, etc.) can disrupt the instrument's effective slit function and wavelength registration through minute variations in the optical path (Noël et al., 2012; Voors et al., 2006). Therefore, research on spectral calibration method is crucial for maintaining the integrity of TEMPO's hyperspectral geostationary orbit measurement data and ensuring stable long-term atmospheric monitoring.

Spectral calibration is essential for retrieving accurate trace gas concentrations from satellite or airborne spectrometers. The pioneering work of Caspar and Chance (Caspar & Chance, 1997) on the Global Ozone Monitoring Experiment (Liu et al., 2005; van Geffen, 2004; van Geffen & van Oss, 2003) developed the first universal method for joint calibration of wavelength and slit-function for Ultraviolet–Visible (UV-VIS) hyperspectral instruments, providing a widely applicable template for atmospheric remote sensing, which can be modified according to specific instrument.

Following this study, a series of Low-Earth-Orbit (LEO) sensors expanded and validated the technology. These included the spectral calibrations of GOME-2 (Cai et al., 2012; Munro et al., 2016), the Ozone Monitoring Instrument (Dirksen et al., 2006; Liu et al., 2010; van den Oord et al., 2006; Voors et al., 2006), the SCanning Imaging Absorption spectroMeter for Atmospheric CHartographY (SCIAMACHY) (Hamidouche & Lichtenberg, 2018), the Ozone Mapping and Profiler Suite (OMPS) (Bak et al., 2017; Seftor et al., 2014), the Orbiting Carbon Obsrvatory-2 (OCO-2) (Sun, Liu, Nowlan, et al., 2017), and the Tropospheric Monitoring Instrument (TROPOMI) (Kleipool et al., 2018; Ludewig et al., 2020). They extended the Caspar and Chance framework to maintain sub-pixel wavelength accuracy over multi-year missions, even under degradation caused by onboard thermal cycling and ionizing radiation. The results demonstrate that a well-designed on-orbit instrument calibration program is crucial for extending the recording length of atmospheric composition data.

Airborne instruments provide a controlled, high-signal environment for prototyping and testing these methods before applying them to satellites. The Airborne Compact Atmospheric Mapper (Liu et al., 2015a, 2015b) and Geostationary Trace Gas and Aerosol Sensor Optimization (GeoTASO) (Nowlan et al., 2016) demonstrate the transfer of laboratory calibration results to in-flight solar source calibration results in the Ultraviolet–Near Infrared (UV–NIR) band. Meanwhile, the Geostationary Coastal and Air Pollution Events (GEO-CAPE) Airborne Simulator (GCAS) adds pre-flight calibration and in-flight solar atlas fitting capabilities, allowing for onboard updates of the lookup table to maintain wavelength offsets within 0.002 nm over ±0.25 K (Nowlan et al., 2018). Recently, MethaneAIR has extended wavelength calibration and slit-function characterization to Short-Wave Infrared (SWIR) (Chan Miller et al., 2024; Conway et al., 2024), demonstrating that similar calibration concepts can support the retrieval of greenhouse gas with an accuracy of parts per million (ppm).

These instruments collectively demonstrate a clear development trajectory: from the initial Caspar–Chance calibration algorithm, to subsequent satellite missions, and then to flexible airborne test platform for the validating and refining new technologies, thereby reducing the development risks of next-generation geostationary orbit sensors, such as TEMPO (Zoogman et al., 2017), the Geostationary Environment Monitoring Spectrometer (Hadjimitsis et al., 2015; Kang et al., 2020), and the Ultraviolet-Visible-Near-Infrared Spectrometer (UVN) (Courrèges-Lacoste et al., 2011; Noël et al., 2012). By focusing on calibration strategies rather than the specifics

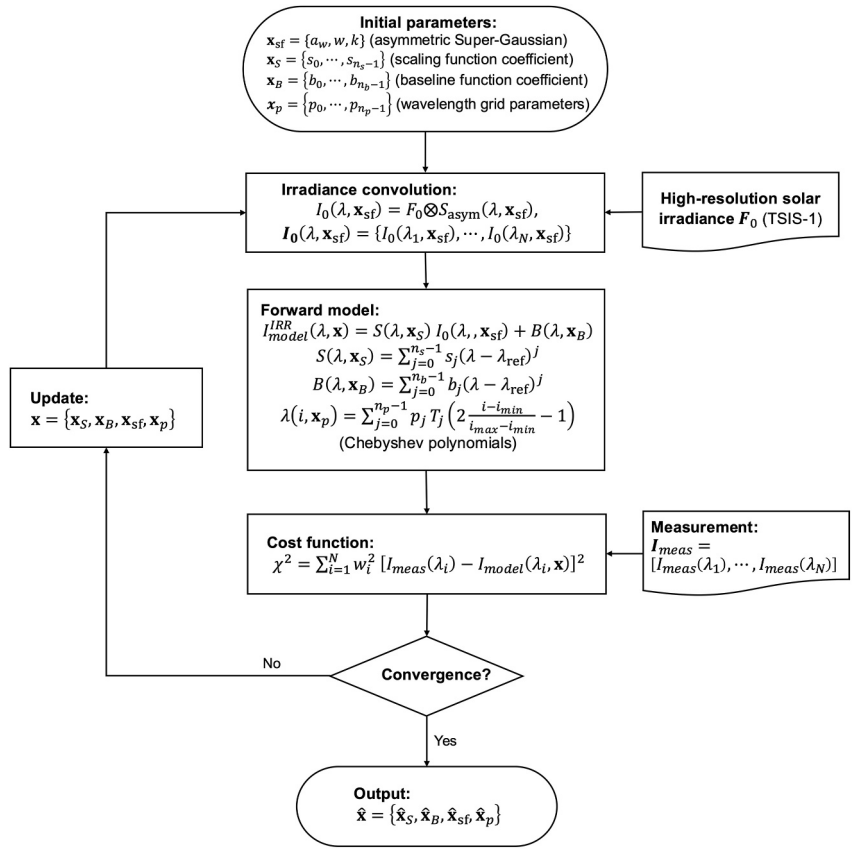

Figure 1. Flowchart of spectral calibration process for solar irradiance.

detail of instrument calibration, we gained transferable knowledge that can be used in the design and maintenance of future missions.

This paper, based on TEMPO Version 3 (V3) data, provides a detailed analysis of the TEMPO V3 spectral calibration algorithm and its time-series spectral performance. After this, in Section 2, the analysis framework will be explained. Sections 3 and 4 discuss the spectral calibration results for irradiance and radiance, respectively, focusing on the problems encountered by the TEMPO algorithm and their solutions. Section 5 explores the trending analysis of calibration results over time, and Section 6 summarizes the conclusions.

2. Methodology

For an overview of TEMPO data and processing workflows, please refer to the Algorithm Theoretical Basis for TEMPO Version 3 Level 0–1 processor (Chong et al., 2026), which includes a summary of the operational spectral calibration process. This paper focuses primarily on the details of the spectral calibration process, including both operational wavelength calibration and offline slit-function inversion test. Figure 1 shows a detailed flowchart of the solar irradiance spectral calibration process, while Figure 2 illustrates the steps of the radiance spectral calibration process.

2.1. Spectral Grid Reconstruction

For spectral calibration, the wavelength grid is typically parameterized as a function of pixel index:

$$\lambda_{i,p} = \lambda_{i,0} + G(i, \boldsymbol{x}_p), \tag{1}$$

where $\lambda_{i,0}$ is the nominal wavelength assigned to pixel i in the pre-launch characterization. If the algorithm directly solves for the absolute wavelength grid, it can be set to zero; if only wavelength changes are fitted, it can

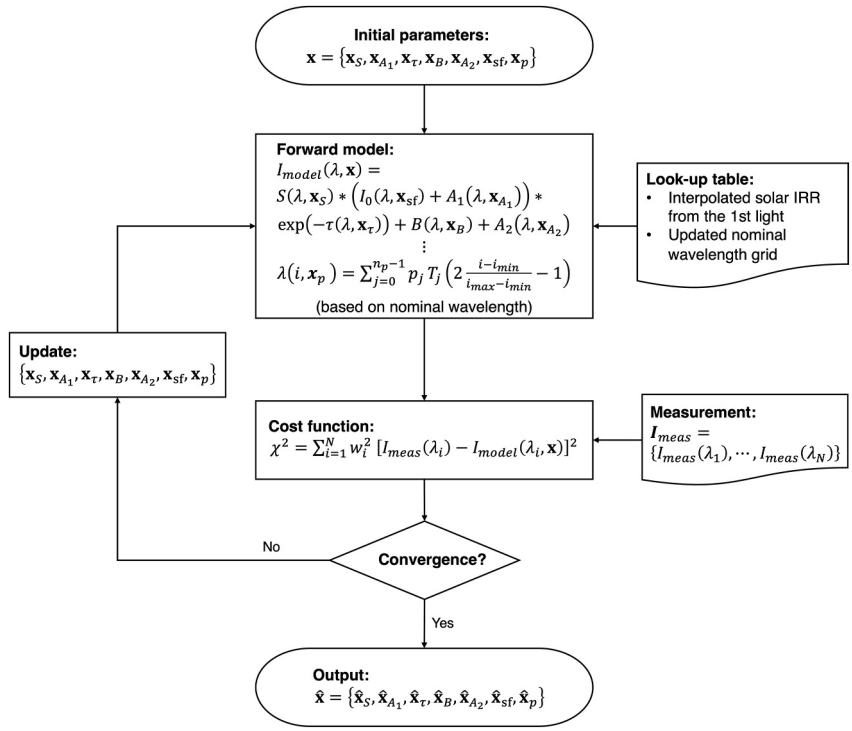

Figure 2. Flowchart of spectral calibration process for Earth-view radiance.

be left as a constant baseline; G represents the wavelength correction or full grid function; i represents the detector pixel index; $\boldsymbol{x}_p$ is a state vector of fitting coefficients:

$$\boldsymbol{x}_p = \{p_0, p_1, \cdots, p_{n_p-1}\}, \tag{2}$$

where $p_0, p_1, \cdots, p_{n_p-1}$ are the corresponding fitting coefficients, and n_p is the total number of polynomial coefficients used in the TEMPO L1b processing. This formula simultaneously achieves absolute spectral calibration and incremental wavelength shift inversion within a unified framework:

1. Absolute spectral calibration: Wavelength assignment refers to the absolute mapping relationship between the detector spectral index i and the physical wavelength $\lambda_{i,p}$, which can be expressed as a Chebyshev polynomial expansion. The wavelength shift is obtained by subtracting the nominal wavelength from the newly obtained wavelength assignment. In this absolute spectral calibration method, the dispersion relation is obtained directly from the spectral fitting of solar irradiance measurements, thus generating an independent wavelength solution for each calibration period. TEMPO operational Level 0–1 processor uses this method to perform wavelength calibration on solar irradiance data.
2. Incremental wavelength shift: This methos directly obtains the relative deviation from the nominal wavelength grid by fitting the observed Earth-view radiance spectra, while keeping the nominal wavelength grid unchanged. The incremental wavelength shift is parameterized as a Chebyshev polynomial function and then added to the nominal wavelength to obtain the updated wavelength grid. This incremental calibration strategy is computationally efficient and particularly suitable for the wavelength calibration of Earth-view radiance measurements, because although the wavelength correction amount for measurements is small, it varies with across track and time.

For pixel index $i \in [i_{\min}, i_{\max}]$, the wavelength is expressed as

$$\lambda(i, \mathbf{x}_p) = \sum_{j=0}^{n_p-1} p_j T_j \left(2\frac{i - i_{\min}}{i_{\max} - i_{\min}} - 1\right), \tag{3}$$

where T represents j-th order Chebyshev polynomials, recursively defined as:

$$\begin{cases} T_0(x) = 1 \\ T_1(x) = x \\ T_{j+1}(x) = 2xT_j(x) - T_{j-1}(x), j \geq 2 \end{cases}. \tag{4}$$

For TEMPO solar irradiance and Earth-view radiance, the UV and VIS regions each contain 1,028 wavelength channels, with a spectral sampling of approximately 0.2 nm. For example, if the entire window of TEMPO is used, and $i_{\min} = 1$ and $i_{\max} = 1028$, then the wavelength grid or shift can be expressed as:

$$\lambda(i) = \sum_{j=0}^{n_p-1} p_j T_j \left(\frac{2i - N + 1}{N - 1} \right), N = 1028. \tag{5}$$

2.2. Forward Model

In the Level 0–1 processor, the slit function (SF) of TEMPO is represented by a super-Gaussian function:

$$S_{\text{asym}}(x) = A_{\text{asym}} \begin{cases} \exp\left(-\left| \frac{x}{w - a_w} \right|^{k - a_k} \right) \text{ for } x \leq 0 \\ \exp\left(-\left| \frac{x}{w + a_w} \right|^{k + a_k} \right) \text{ for } x > 0 \end{cases}, \tag{6}$$

where k is the shape parameter, w is the half-width at 1/e (hw1e), and a_k and a_w are additional asymmetric parameters. The scaling coefficient is given by:

$$A_{\text{asym}} = \frac{k}{2w\Gamma(1/k)}, \tag{7}$$

where Γ represents the gamma function (Beirle et al., 2017). When $k = 2$, for symmetric cases, this function simplifies to a standard Gaussian function. In the TEMPO V3 Level 0–1 processor, only three slit-function parameters are considered, where $a_k = 0$, thus obtaining the parameter set:

$$\mathbf{x}_{\text{sf}} = (a_w, w, k)^T. \tag{8}$$

The convolved reference solar spectrum is calculated as follows:

$$I_0(\lambda, \mathbf{x}_{\text{sf}}) = F_0 \bigotimes S_{\text{asym}}(\lambda, \mathbf{x}_{\text{sf}}), \tag{9}$$

where F_0 represents the high-resolution solar irradiance data set, and $\bigotimes$ denotes convolution. According, the resulting discrete convolved spectrum can be expressed as:

$$\boldsymbol{I_0}(\lambda, \mathbf{x}_{\text{sf}}) = \{I_0(\lambda_1, \mathbf{x}_{\text{sf}}), \cdots, I_0(\lambda_n, \mathbf{x}_{\text{sf}})\}, \tag{10}$$

where n is the number of bands used in the convolution.

For spectral calibration in the Level 0–1 processor, the modeled solar irradiance and Earth-view radiance follow the unified equation:

$$I_{\text{model}}(\lambda, \mathbf{x}) = S(\lambda, \mathbf{x}_S)\left(I_0(\lambda, \mathbf{x}_{\text{sf}}) + A_1(\lambda, \mathbf{x}_{A_1})\right) \exp(-\tau(\lambda, \mathbf{x}_\tau)) + B(\lambda, \mathbf{x}_B) + A_2(\lambda, \mathbf{x}_{A_2}), \tag{11}$$

where I_0 is the convolved reference solar spectrum, A_1 represents pre-absorption additive corrections, S is the scaling function, B is the baseline function, τ corresponds to trace gas absorption, and A_2 accounts for post-absorption additive correction. The state vector is:

$$\mathbf{x} = \{\mathbf{x}_S, \mathbf{x}_{A_1}, \mathbf{x}_\tau, \mathbf{x}_B, \mathbf{x}_{A_2}, \mathbf{x}_{\text{sf}}, \mathbf{x}_p\} \tag{12}$$

where $\mathbf{x}_{\text{sf}}$ and $\mathbf{x}_p$ are the previously defined slit function and wavelength grid parameters. Version 2 of the Total and Spectral Solar Irradiance Sensor-1 (TSIS-1) Hybrid Solar Reference Spectrum (HSRS) is used as the reference solar spectrum (Coddington et al., 2023).

For Earth-view radiance, the full forward model described in Eq. (11) is applied without any simplification, thus enabling the retrieval of all relevant physical and instrumental parameters, including atmospheric absorption, additive corrections, and wavelength-dependent scaling. Conversely, for solar irradiance, the terms A_1, A_2 and τ are all set to zero, thus simplifying the forward model to:

$$I^{\text{IRR}}_{\text{model}}(\lambda, \mathbf{x}) = S(\lambda, \mathbf{x}_S)\, I_0(\lambda, \mathbf{x}_{\text{sf}}) + B(\lambda, \mathbf{x}_B), \tag{13}$$

where the fitting coefficient vector is:

$$\mathbf{x} = \{\mathbf{x}_S, \mathbf{x}_B, \mathbf{x}_{\text{sf}}, \mathbf{x}_p\}. \tag{14}$$

Specifically, both the scaling function and the baseline function can be reconstructed using polynomial expansions, as shown below:

$$\begin{cases} S(\lambda, \mathbf{x}_S) = \sum_{j=0}^{n_s-1} s_j (\lambda - \lambda_{\text{ref}})^j \\ B(\lambda, \mathbf{x}_B) = \sum_{j=0}^{n_b-1} b_j (\lambda - \lambda_{\text{ref}})^j \end{cases}, \tag{15}$$

where the fitting polynomial coefficients are defined as:

$$\begin{cases} \mathbf{x}_S = \{s_0, \cdots, s_{n_s-1}\} \\ \mathbf{x}_B = \{b_0, \cdots, b_{n_b-1}\} \end{cases}. \tag{16}$$

Here, λ_{ref} represents the reference wavelength, while n_s and n_b are the number of coefficients in the scaling function of $S(\lambda, \mathbf{x}_S)$ and the baseline function $B(\lambda, \mathbf{x}_B)$, respectively. Other functions, such as $A_1(\lambda, \mathbf{x}_{A_1})$ and $A_2(\lambda, \mathbf{x}_{A_2})$, can also be represented by polynomial expansions. However, the term $\tau(\lambda, \mathbf{x}_\tau)$ is usually derived using the Beer-Lambert law.

2.3. Spectral Fitting and Iteration

For spectral fitting, the cost function can be expressed as:

$$\chi^2 = \sum_{i=1}^{n} w_i^2 \left[I_{\text{meas}}(\lambda_i) - I_{\text{model}}(\lambda_i, \mathbf{x})\right]^2, (i = 1, \cdots, n), \tag{17}$$

where I_{meas} denotes the irradiance or radiance observed by TEMPO, I_{model} corresponds to the output of the forward model, and n is the number of wavelengths used in the fitting process. Furthermore, the weighting factor w_i is defined as

$$w_i = \frac{1}{\alpha \epsilon_i}, \tag{18}$$

where ϵ_i represents the irradiance or radiance error, and α is a scale factor used for normalization. The measurement errors ϵ_i is obtained from the uncertainty variables provided in the TEMPO Level 1 data, where the irradiance error (units: photons $\cdot$ s^{-1} cm^{-2} nm^{-1}) is for solar-irradiance fitting and radiance error (units: photons $\cdot$ s^{-1} cm^{-2} nm^{-1} sr^{-1}) is for Earth-view radiance fitting. These weights ensure that spectral samples with greater uncertainties contribute less to the χ^2 cost function in Equation 17.

We use MPFIT, a C library that implements the NINPACK-1 Levenberg-Marquardt least-squares algorithm (Markwardt, 2012), to minimize the cost function. By setting the relative chi-square convergence criterion, the relative parameter convergence criterion, and the threshed for the maximum number of iterations, the final retrieved parameter values are obtained once convergence or the iteration limit is reached.

Figure 1 shows a detailed flowchart of the solar irradiance spectral calibration process. The assigned wavelength for each pixel is explicitly defined as the centroid of the slit function. This relationship remains constant throughout the iterative optimization to ensure consistency between the wavelength solution and slit-function parameters. After spectral fitting of solar irradiance, the retrieved state vector is expressed as:

$$\hat{\mathbf{x}} = \{\hat{\mathbf{x}}_S, \hat{\mathbf{x}}_B, \hat{\mathbf{x}}_{\mathrm{sf}}, \hat{\mathbf{x}}_p\}, \tag{19}$$

and the wavelength grid is calculated using Equation 5.

In the TEMPO Version 3 Level 0–1 operational processor, irradiance wavelength calibration employs a spectrally invariant (wavelength-averaged) asymmetric super-Gaussian slit function. This wavelength-averaged configuration is primarily used to reduce the dimensionality of the fitting process and improve computational efficiency. Furthermore, the fixed spectrally invariant slit function provides greater numerical stability and robustness during operational processing, avoiding potential overfitting and interdependence among wavelength-dependent parameters.

Meanwhile, Figure 2 shows a simplified flowchart of the radiance wavelength calibration, where the retrieved state vector is:

$$\hat{\mathbf{x}} = \{\hat{\mathbf{x}}_S, \hat{\mathbf{x}}_{A_1}, \hat{\mathbf{x}}_\tau, \hat{\mathbf{x}}_B, \hat{\mathbf{x}}_{A_2}, \hat{\mathbf{x}}_{\mathrm{sf}}, \hat{\mathbf{x}}_p\}. \tag{20}$$

Here, radiance spectral calibration is performed relative to the wavelength grid obtained from the most recent solar irradiance wavelength calibration, using the interpolated first-light solar irradiance as the reference spectrum. This method simplifies the operation process by eliminating the need to repeatedly update the convolutional solar irradiance lookup tables, taking into account the systematic radiometric errors that exists in both irradiance and radiance, ultimately achieving more efficient and accurate spectral fitting.

2.4. Offline Retrieval of Slit Functions in Narrow Spectral Windows

The TEMPO Version 3 Level 0–1 operational processor employs a fixed asymmetric super-Gaussian slit function, assumed to be spectrally invariant, with its wavelength-averaged parameters archived in the publicly released Version 3 L1b irradiance data. In contrast, the method described in this section investigates wavelength-dependent slit functions within selected narrow spectral windows. Since this method is not yet incorporated into the operational (online) pipeline, it is referred to as offline processing.

Pre-launch characterization analysis provides super-Gaussian slit functions for each TEMPO cross-track pixel at nine UV wavelengths (297.8, 310, 320, 330, 355, 390, 425, 460, and 488.2 nm) and five VIS wavelengths (541.8, 605, 640, 675, and 736 nm), which are interpolated to individual detector pixels for on-orbit use. To assess potential post-launch variations, we perform offline re-estimation of slit functions within selected narrow spectral windows from measured V3 L1b solar irradiance spectra and analyze their temporal trends. The corresponding workflow is as follows:

1. Narrow-window definition: Nine UV windows and seven VIS windows are selected to cover the pre-flight calibration wavelengths; two additional VIS windows are located at 575 and 705 nm, respectively, to strengthen interpolation constraints. Table 1 lists the nominal channels, pixel start indices, fitted-pixel

Table 1
UV and VIS Channels (Small Spectral Windows) Used for Slit Function Retrievals

	UV				VIS			
No.	Channel (nm)	Pixel start indices	Fitted-pixel No.	Coverage (nm)	Channel (nm)	Pixel start indices	Fitted-pixel No.	Coverage (nm)
1	297.8	11	200	294.1–333.7	541.8	11	200	539.7–579.2
2	310	31	200	296.1–335.7	575	25	319	542.4–605.6
3	320	94	200	310.5–350.1	605	193	329	575.7–640.8
4	330	145	200	320.6–360.2	640	344	355	605.6–675.8
5	355	195	301	330.5–390.1	675	522	300	640.8–700.1
6	390	322	353	355.7–425.5	705	699	300	675.8–735.1
7	425	499	353	390.7–460.5	736	851	168	705.9–739.1
8	460	675	320	425.5–488.8				
9	488.2	852	167	460.5–493.6				

numbers, and approximate spectral coverages. A small amount of overlap between adjacent windows is allowed to ensure smooth transitions and stable retrieval performance.

2. Parameter retrieval: Within each spectral window, joint spectral fitting is performed to simultaneously retrieve a set of wavelength-independent slit-function parameters and a small shift relative to the nominal wavelength grid. The slit function within each narrow window is considered spectrally invariant.
3. Spectral interpolation: Successful pixel-level solution is performed across the entire UV or VIS range using piecewise cubic Hermite interpolation (pchip); pixels that fail quality control are excluded from the fitting.
4. Outlier filtering and storage: Interpolated parameter values are smoothed along each cross-track to suppress residual outliers. The final slit-function parameters are archived in Network Common Data Form (NetCDF-4) format for potential processing and applications.

This piecewise approach allows for updating and tracking of the TEMPO slit functions throughout the mission without rerunning the full bandpass property analysis. Tests using parameter combinations $(a_w, w, k)^T$ and $(w, k)^T$ show that the retrieval of a_w is unstable and has relatively large uncertainties, which will be discussed in Section 3.3. Therefore, the final offline fitting constrains the slit function to a symmetric function by setting $a_w = 0$ and $a_k = 0$.

In this study, the interpolation and smoothing of slit-function parameters are performed in the initial offline tests using a simplified method. The potential effects of inter-parameter correlation and area normalization are not explicitly considered here, but these effects will be addressed in future work through a more physically constrained smoothing framework.

3. Wavelength Calibration Results for Irradiance

3.1. Solar Irradiance Spectral Fitting

To evaluate and optimize the irradiance spectral calibration, we utilize solar irradiance data first observed by TEMPO on 1 August 2023. The solar reference spectrum published by the Smithsonian Astrophysical Observatory (SAO) in 2010 (SAO2010) (Chance & Kurucz, 2010) and Version 2 of the TSIS-1 HSRS (Coddington et al., 2023) are used as reference solar spectra data set for spectral fitting.

TEMPO solar irradiance is measured in photon irradiance (units: photons $\cdot\, s^{-1}\ cm^{-2}\ nm^{-1}$), while TSIS-1 HSRS data is measured in irradiance (units: $W \cdot m^{-2}\ nm^{-1}$). Therefore, we use the following equation to convert spectral irradiance L_λ to photon irradiance $L_{q\lambda}$:

$$L_{q\lambda} = \frac{L_\lambda\, \lambda}{h\, c}, \tag{21}$$

where λ is the wavelength (in meters), h is Planck's constant (in J·s), c is the speed of light (m/s).

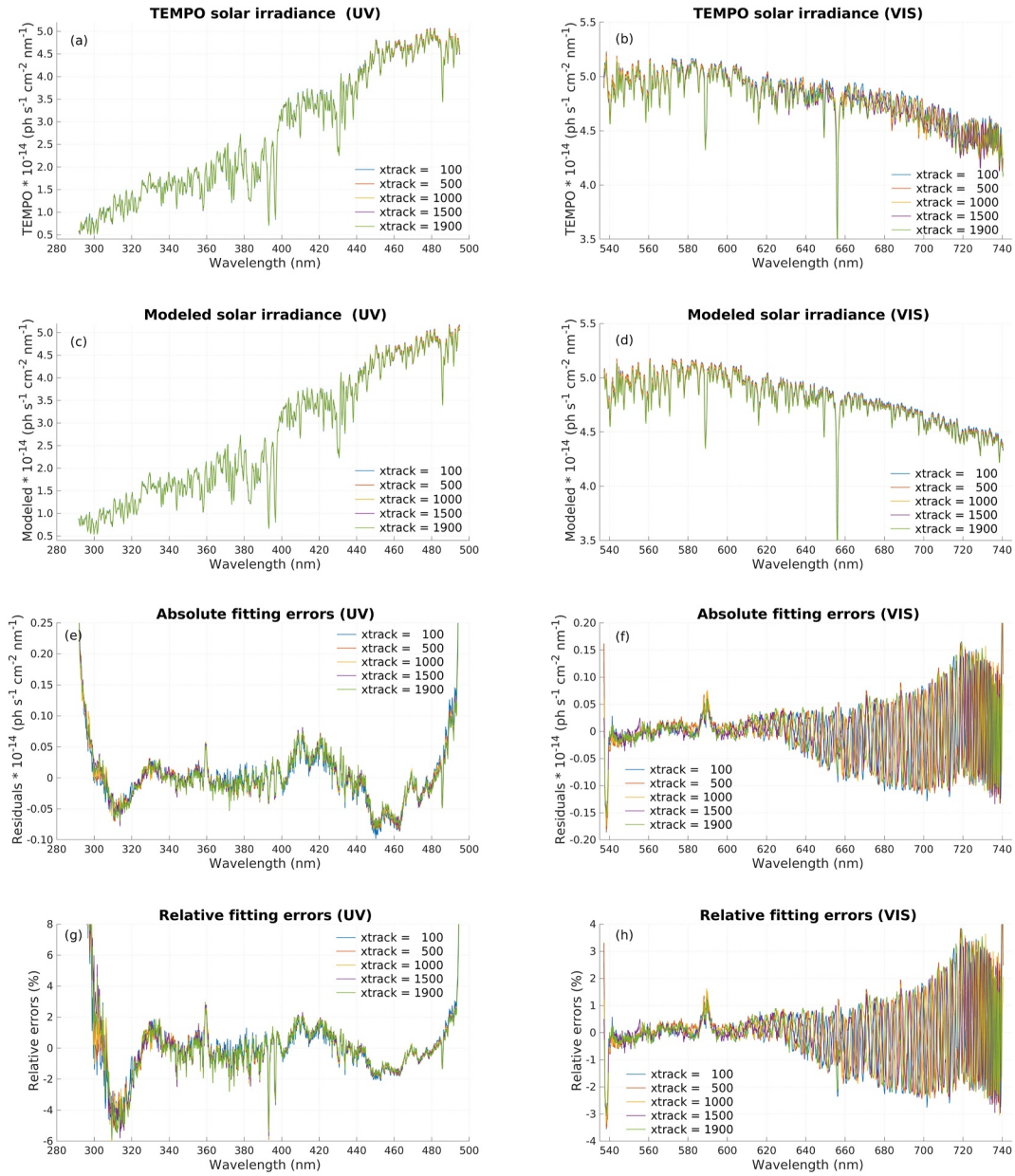

Figure 3. Comparison of TEMPO solar irradiance and simulated fitted spectra results using the reference TSIS-1 Hybrid Solar Reference Spectrum as a function of wavelength in UV (left panel) and VIS (right panel) for different cross track (xtrack) pixels, along with the corresponding fitting errors. (a, b): TEMPO-measured solar irradiance from first light, expressed in photon irradiance with the unit of photons/$\left(s \cdot cm^2 \cdot nm\right)$ and scale factor of 10^{-14}. (c, d): Modeled solar irradiance (e, f): Absolute fitting errors of solar irradiance, obtained as the modeled spectrum minus the TEMPO spectrum. (g, h): Relative fitting errors of solar irradiance, calculated as the difference between the modeled and TEMPO spectra, and normalized by the TEMPO spectrum.

For the irradiance wavelength calibration, we discard the 10 outermost detector channels at both the short and long wavelength ends to reduce the high edge noise typically observed near spectral boundaries; that is, we exclude the first 10 and last 10 channels, retaining 1,008 central channels for the complete spectral analysis in the UV and VIS region, respectively.

Figure 3 directly compares the measured and modeled (simulated) solar irradiance spectra at five cross-track positions observed by TEMPO in the UV and VIS regions during the first light observation. The simulated spectra are generated using the TSIS-1 HSRS as the reference solar spectrum. Panels (a, b) show the measured

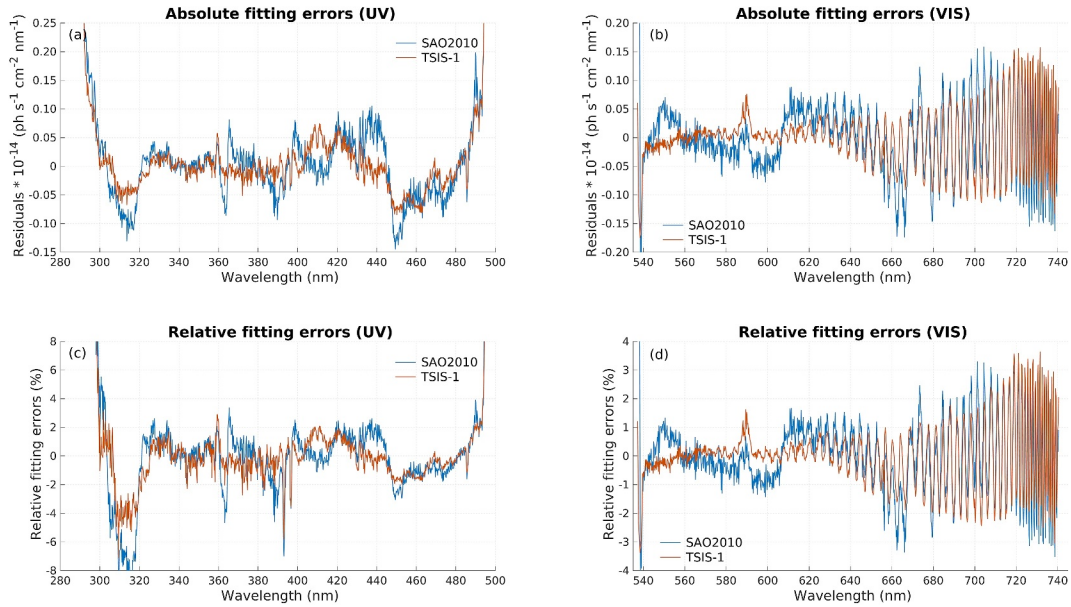

Figure 4. Comparison of solar irradiance fitting errors as a function of wavelength using SAO2010 and TSIS-1 Hybrid Solar Reference Spectrum as reference spectra in UV (left panel) and VIS (right panel) (a, b): Absolute fitting errors (c, d): Relative fitting errors. The solar irradiance spectra for comparison were selected from xtrack = 1,000 in the first-light data.

TEMPO solar irradiance (version 3) in the UV and VIS ranges, respectively. Panels (c–d) represent the corresponding modeled irradiance spectra, which are coupled with wavelength-averaged slit functions for the UV and VIS, respectively, retrieved simultaneously. The small differences in solar irradiance observed by TEMPO at different across-track positions are mainly caused by residual radiometric calibration uncertainties, resulting in slight variations in the fitting coefficients of the modeled solar irradiance spectra derived from Equation 13. Panels (e, f) display the absolute residuals of the measured and modeled spectra. The deviations are larger near the spectral edges and in regions with sharp spectral features. Panels (g, h) show the relative fitting errors, mostly within ±2% in the central part of the spectrum, but with a slight cross-track dependency still present. These results confirm the performance of forward modeling based on wavelength-averaged cross-track dependent slit functions in the UV and VIS spectral regions. The slight biases in TEMPO solar irradiance in the 300–310 nm region are likely related to small residual uncertainties in radiometric calibration. This effect may propagate to trace gas retrievals (e.g., ozone) when corresponding Earth-view radiance data is used. The larger fitting residuals beyond 630 nm in the VIS are due to known etalon structures that were not corrected for in the L1b solar irradiance data.

To quantitatively assess the impact of different reference solar spectra on the TEMPO spectral fitting results, we compare the errors as a function of wavelength when fitting solar irradiance using SAO2010 and TSIS-1 HSRS in the UV and VIS regions, as shown in Figure 4. Correspondingly, Table 2 lists the mean absolute error (MAE) and mean percentage error (MPE) of spectral fitting using different numbers of Chebyshev polynomials with SAO2010 and TSIS-1 HSRS as reference spectra. The results clearly show that the MAE and MPE are significantly smaller when using TSIS-1 HSRS compared to SAO2010. Consequently, we select TSIS-1 HSRS as the high-resolution solar reference spectrum for spectral calibration.

3.2. Wavelength Shift Relative to Prelaunch Calibration

Taking the first light irradiance spectral calibration as an example, Figure 5 shows the test results of wavelength shift derived by performing absolute spectral calibration of the first-light solar irradiance data using different numbers of Chebyshev polynomial coefficients (n_p) and then subtracting the prelaunch wavelength assignment. The wavelength shift is obtained as

$$\Delta\lambda(i,n_p) = \lambda_{\text{first-light}}(i,n_p) - \lambda_{\text{prelaunch}}(i), (i = 1,\cdots,1028), \quad (22)$$

Table 2
Comparison of the Fitting Errors for Different Numbers of Chebyshev Polynomials Coefficients, Using SAO2010 and TSIS-1 Hybrid Solar Reference Spectrum as Reference Solar Spectra

		SAO2010		TSIS-1 HSRS	
	n_p	UV	VIS	UV	VIS
MAE	2	0.047653	0.053550	0.037654	0.043913
	3	0.047645	0.053481	0.037643	0.043856
	4	0.047646	0.053465	0.037647	0.043824
MPE (%)	2	2.3644	1.1053	1.6070	0.9214
	3	2.3644	1.1039	1.6071	0.9201
	4	2.3650	1.1035	1.6073	0.9195

where $\lambda(i,n_p)$ represents the absolute wavelength assignment determined from spectral calibration with a given n_p, and $\Delta\lambda(i,n_p)$ denotes the relative difference between the on-orbit and prelaunch wavelength solutions. For panel (a, b), when lower-order ($n_p \leq 4$) Chebyshev polynomials are used, the retrieved wavelength changes remain relatively stable. However, when higher-order ($n_p > 5$) polynomials are applied, the Runge Phenomenon occurs, leading to oscillations at the edges or within some spectral intervals, particularly in the VIS region. For panel (c, d), the pronounced curvature primarily reflects the residual wavelength differences between the two independent calibrations, rather than the nonlinearity of the wavelength assignment itself.

Here, a fitting failure is defined as the optimization process in the MPFIT (MINPACK-1 least squares fitting library in C) toolbox failing to converge to the required threshold, resulting in a default wavelength shift of zero. While wavelength shifts among cross-track pixels in the UV region exhibit an approximately uniform spectral displacement, those in the VIS region display more complex variations partly due to the difficulty in fitting the etaloning structures at longer wavelengths.

To ensure robust performance in terms of both spectral fitting accuracy and pixel-level stability, we adopt carefully selected parameters for irradiance spectral calibration. Based on comprehensive testing, the spectral calibration is configured with a first-order Chebyshev polynomial fit ($n_p = 2$) for the UV region and second order ($n_p = 3$) for the VIS region. A detailed time-trend analysis of wavelength shift trends following the first light observation will be discussed in Section 5.

3.3. Offline Slit Function Retrieval Results

Figure 6 compares the normalized prelaunch and first-light slit functions, modeled using a super-Gaussian function shape, at selected wavelengths in both the UV and VIS spectral regions. The retrieved parameters

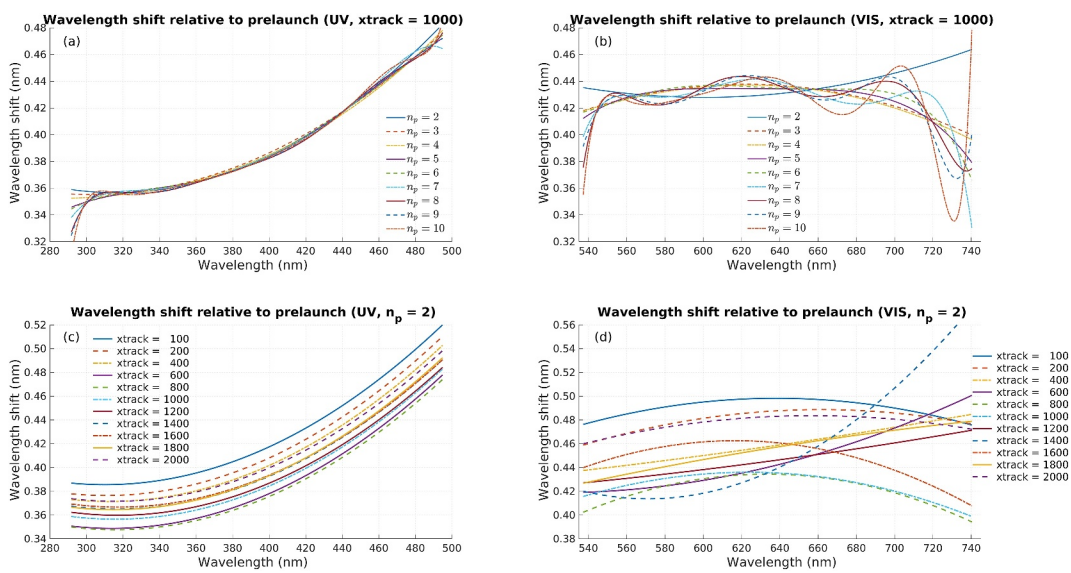

Figure 5. Test results of wavelength change in the first-light solar irradiance calibration relative to the prelaunch wavelength assignment for the UV (left panel) and VIS (right panel) spectral ranges (a, b) Wavelength changes at xtrack = 1,000 obtained by performing absolute spectral calibration of the first-light data using different number of Chebyshev polynomial coefficients. (c, d): Across-track (xtrack) distributions of wavelength changes derived with a fixed first-order Chebyshev expansion ($n_p = 2$). The across-track positions were selected to better illustrate the wavelength-shift variations among different across-track positions and to ensure full coverage of most across-track differences. These wavelength shifts are calculated as the different between the first light and prelaunch wavelength assignments, to illustrate the effect of polynomial order and spatial variation.

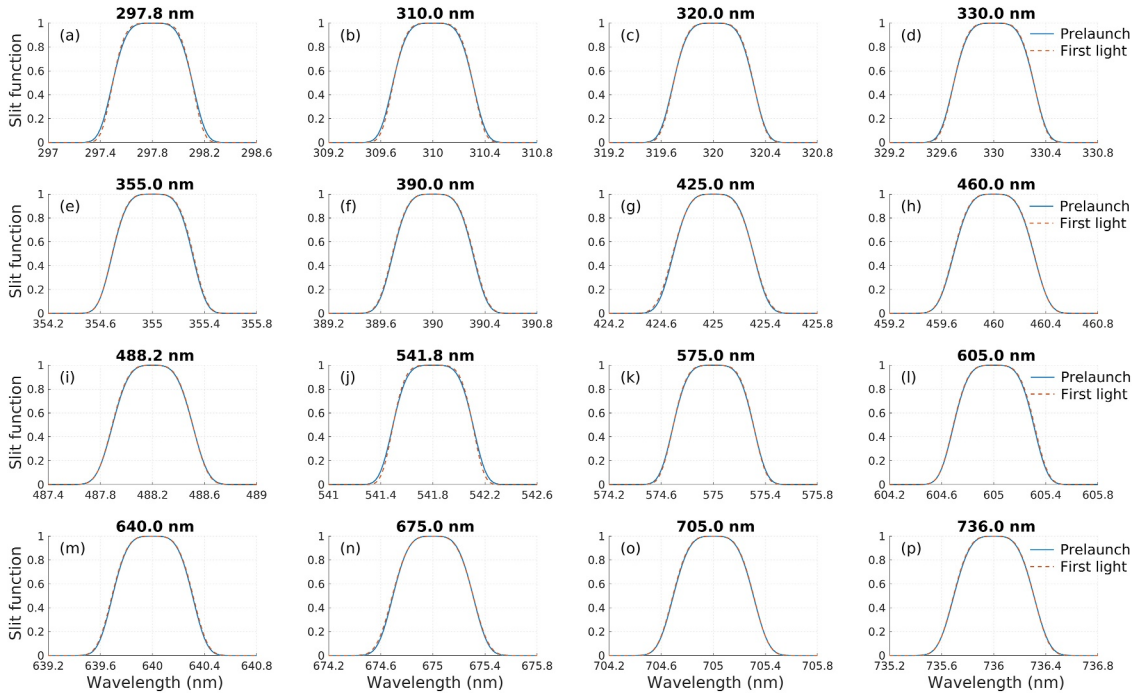

Figure 6. Comparison of normalized slit function (super-Gaussian shape) between prelaunch and retrieved results from first light (a–i): Nine wavelength channels in the UV (j–p): Seven wavelength channels in the VIS.

include the shape parameter (k), the half-width at 1/e (hw1e) parameter (w), and the asymmetry parameter of w (a_w). Overall, the retrieved slit functions show good agreement with their prelaunch counterparts, indicating only minor changes in instrument slit characteristics after launch.

Figure 7 illustrates the interpolation of slit function parameters along the wavelength axis and their smoothing along the cross-track axis, based on the retrievals from small spectral windows. For wavelength interpolation, the MATLAB 1-D interpolation function "interp1" has been used, and three interpolation methods are tested: piecewise linear ("linear"), cubic spline ("spline"), and cubic Hermite polynomial ("pchip") interpolations (MathWorks, 2024). Among them, cubic Hermite interpolation achieves smoother transitions than linear interpolation and exhibits more stable extrapolation behavior than cubic spline interpolation, therefore, it has been chosen for wavelength interpolation in both the UV and VIS regions.

To evaluate the robustness of the interpolation method, we performed sensitivity tests by temporarily removing one or two spectral windows (e.g., the second and penultimate). As shown in Figures 7a–7d, the interpolated curves for the UV region remain almost unchanged when these windows are excluded, indicating the strong stability of the "pchip" interpolation. In contrast, a larger deviation appears near the spectral boundaries in the VIS region, because the slit-function parameters retrieved from the first and last small windows tend to have higher uncertainties. Therefore, we added additional small windows at both edges of the VIS spectral range to better constrain the interpolation and reduce boundary-related errors.

For cross-track smoothing, we applied MATLAB's "smoothdata" function and combined it with a robust locally weighted regression ("rlowess") method to suppress random noise and outliers generated by wavelength interpolation while preserving true spatial variability (Cleveland & Devlin, 1988). Based on the stability of the root mean square error of the residuals and the reduction in the variability of the first derivative, the smoothing strength was empirically optimized to ensure that the results are sufficiently smooth while avoiding over-suppression of true structural changes. This approach guarantees a continuous and physically consistent slit function data set organized on a two-dimensional wavelength and cross-track position grid.

Figure 8 compares the slit function parameters obtained from the prelaunch and first-light retrieval across the wavelength and cross-track position grid in both the UV and VIS regions. Notably, the asymmetric parameter a_w is much smaller than k and w, with its absolute value typically below 0.01 in the UV and below 0.06 in the VIS.

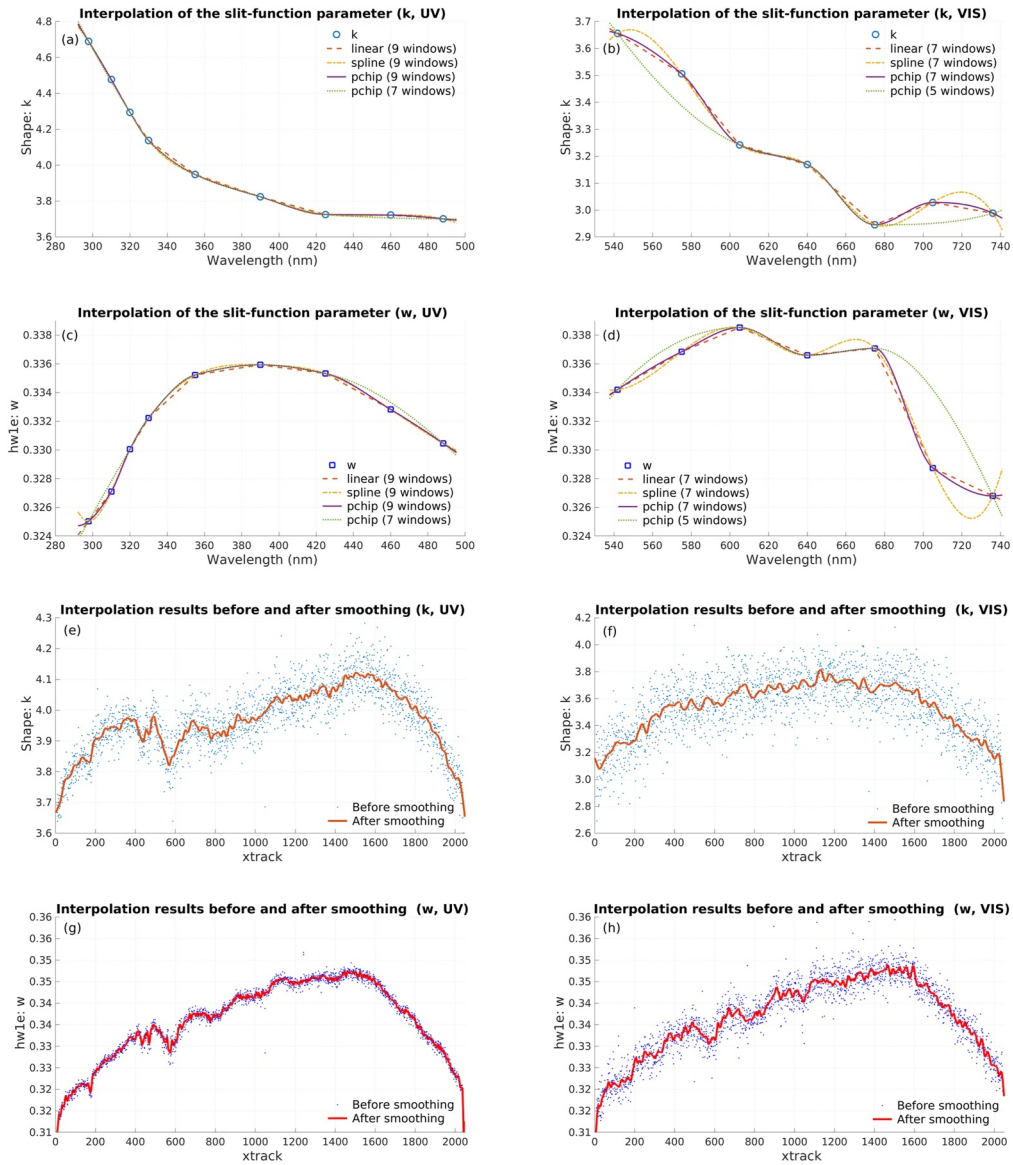

Figure 7. Interpolation and smoothing of slit function parameters based on the retrieved results from small spectral windows in the UV (left panels) and VIS (right panels) (a–d): Interpolation of the slit-function parameters (k, w) along the wavelength axis, using the averaged values over all cross-track positions to present their spectral-trend behavior. Three methods are used for interpolation: "linear" (piecewise linear), "pchip" (cubic Hermite polynomial), and "spline" (cubic spline).The markers indicate the initial retrievals from nine (UV) and seven (VIS) small spectral windows, respectively. "Pchip (7 windows)" and "pchip (5 windows)" denote cubic-Hermite interpolating excluding the second and the penultimate windows (e–h): Smoothed versions of the interpolated parameters (k, w) along the cross-track direction, with the selected spectral indices of 514 (UV) and 200 (VIS). These indices were chosen to cover a wider dynamic range of slit-function parameter values, thus testing the effectiveness of the smoothing method. The robust locally weighted regression method ("rlowess") in the MATLAB's "smoothdata" function was applied to suppress random noise.

Retrieving a_w is challenging due to the inherent correlation between these parameters, which can lead to potential noise in the retrieval of k and w. To mitigate this issue, we choose to retrieve only k and w, and set a_w and a_k to 0 in the small spectral windows analysis. As listed in Table 3, setting $a_w = 0$ (symmetric case) only causes a small change in the retrieved slit-function parameters. The average difference between the symmetric and asymmetric retrievals are less than 0.05 for the shape (k) and below 0.002 for the width (w), indicating that the overall patterns in Figure 8 remain almost unchanged after enforcing symmetry. The implications of this choice and further trending analysis will be discussed in Section 5.

10.1029/2025EA004637

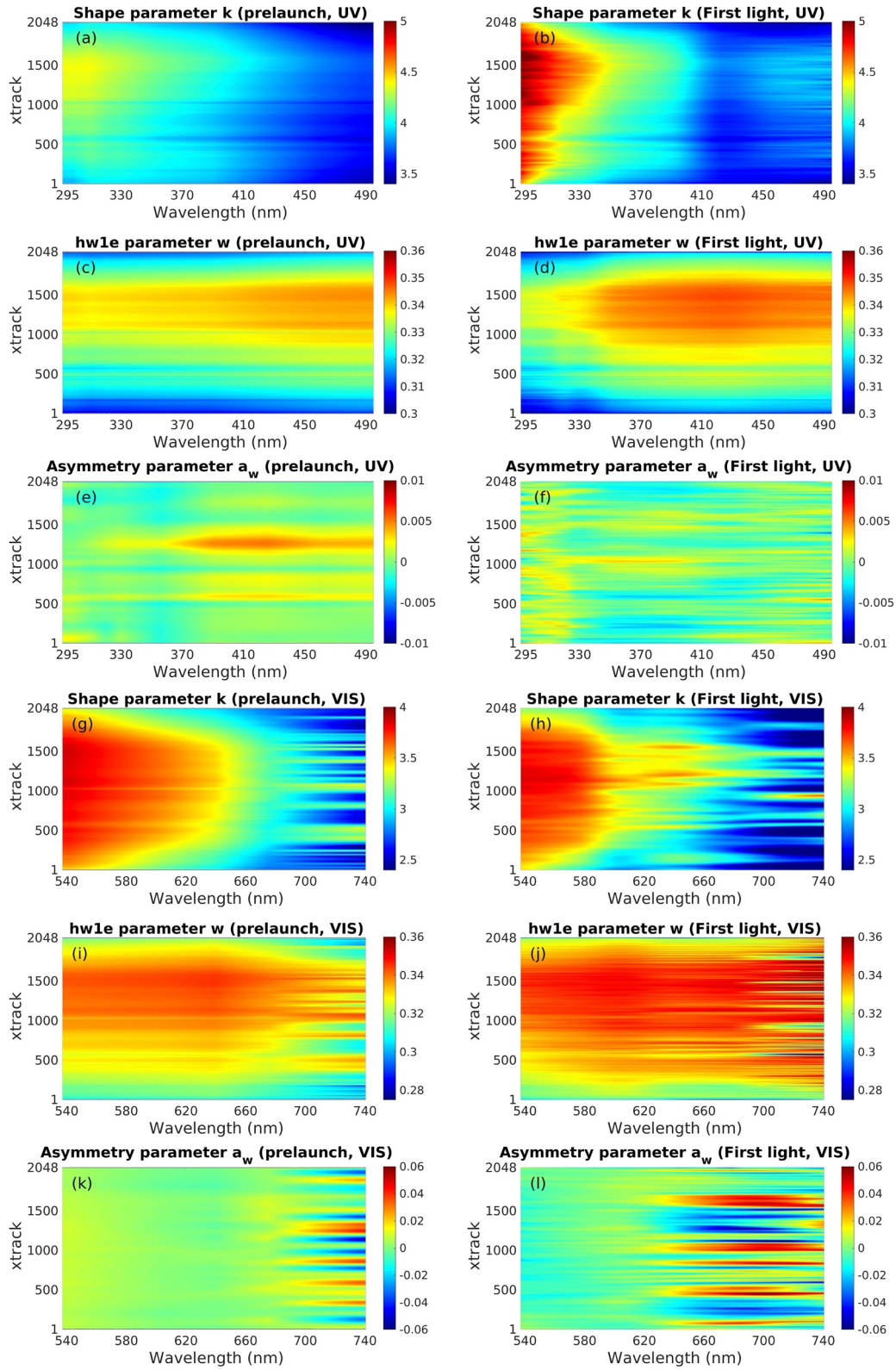

Figure 8. Comparison of mesh-grid slit function parameters (k, w, a_w) between prelaunch (left panel) and first-light retrievals (right panel) in UV (a–f) and VIS (g–l).

Table 3
Mean and Standard Deviation of the Differences in Slit-Function Shape (k) and hw1e (w) Parameters Between the Symmetric ($a_w = 0$) and Asymmetric ($a_w \neq 0$) Cases, Based on the Offline Slit-Function Retrieval Results From the First-Light TEMPO Solar Irradiance Shown in Figure 8

	UV		VIS	
Parameter	mean	std	mean	std
Shape (k)	0.0011	0.0240	0.0403	0.0988
hw1e (w)	−0.00004	0.0008	0.0011	0.0114

4. Wavelength Calibration Results for Radiance

4.1. Full-Spectral-Window Scene Inhomogeneity Assessment

After the nominal spectral grid is updated using the latest TEMPO solar irradiance spectral calibration, a similar spectral shift must be derived for the radiance measurements via a dedicated wavelength spectral calibration. When using the entire spectral window, we follow the same criteria as the irradiance calibration, limiting the radiance calibration to the central 1,008 channels. Figure 9 shows, for the full UV spectral window, the spatial pattern and corresponding histogram of the first two Chebyshev-polynomial coefficients ($n_p = 2$) that quantify the spectral shift relative to the updated nominal spectral grid for every Earth-view radiance pixel in a single granule. For example, the figure further distinguishes pixels labeled as homogeneous or inhomogeneous, using thresholds derived from the mean and standard deviation of granule's histogram.

The threshold for determining the homogeneous and inhomogeneous pixels is defined as follows:

$$\varepsilon_{p_i} = \overline{p_i} \pm \sigma_{p_i}, i = 0 \; or \; 1, \tag{23}$$

with the classification criteria:

$$\begin{cases} \overline{p_i} - \sigma_{p_i} \leq p_i \leq \overline{p_i} + \sigma_{p_i}, & \text{homogeneity} \\ p_i < \overline{p_i} - \sigma_{p_i} \parallel p_i > \overline{p_i} + \sigma_{p_i}, & \text{inhomogeneity} \end{cases}, \tag{24}$$

where $\overline{p_i}$ is the mean of the ith coefficient, and σ_{p_i} is its standard deviation. Since the number of inhomogeneity pixels is usually different when using ε_{p_0} and ε_{p_1}, for simplicity, the threshold with a larger number of inhomogeneous pixels is chosen.

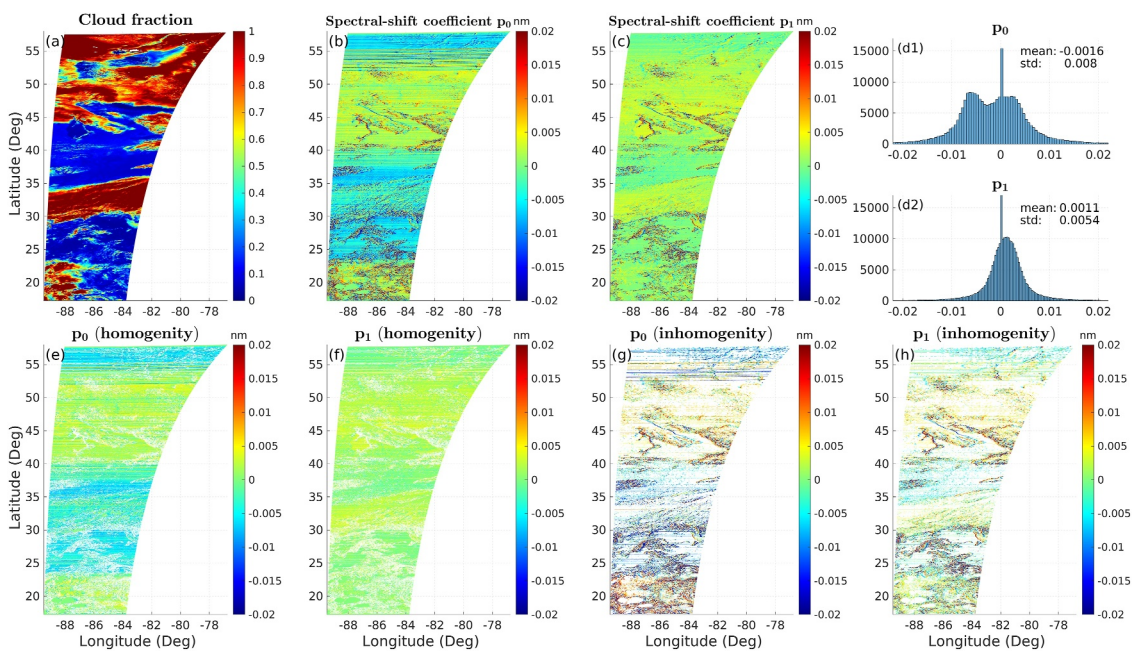

Figure 9. Spatial maps and histograms of the first two Chebyshev-polynomial coefficients that describe the wavelength spectral shift relative to the updated nominal grid (calibrated over the full UV spectral window) for every TEMPO Earth-view radiance pixel in a granule, together with the associated homogeneous/inhomogeneous pixel masks and cloud-fraction field for that granule. Panels: (a) cloud-fraction map, (b, c) spatial distribution of the first and second Chebyshev-polynomial coefficients ($n_p = 2$) derived from the UV window; (d) joint histogram of those two coefficients; (e, f) pixels classified as homogeneous using the histogram mean ± standard deviation (std) threshold, (g, h) pixels classified as inhomogeneous (outside mean ± std).

Table 4
Wavelength Channels Used in Three Typical Radiance Spectral Calibration Approaches (n_p Indicates the Number of Chebyshev Polynomial Coefficients)

Wavelength channels	UV	VIS	Number of wavelengths	n_p
Entire spectrum	293–493 nm	537–741 nm	1,008	2
Small windows	Centered at 303.8, 323.6, 343.4, 363.2, 383.0, 402.8, 422.6, 442.4, 462.2, 482.0 nm with ∼20 nm range	Centered at 549.4, 569.2, 589.0, 608.7, 628.5, 648.3, 668.1, 687.9, 707.6, 727.4 nm with ∼20 nm range	100 for each	1
Spectral intervals	2, 3, 4, 5, and 10 intervals in 293–493 nm	2, 3, 4, 5, and 10 intervals in 537–741 nm	504, 336, 252, 202, 101	2

Comparison with TEMPO's cloud fraction in the CLDO4 product (Wang et al., 2025) reveals that the distribution of inhomogeneous pixels is consistent with cloud boundaries. Inhomogeneity is minimal in areas with clear skies or complete cloud coverage, while most inhomogeneous pixels are located near cloud boundaries. Therefore, the cloud fraction product can also be used as an indicator of scene inhomogeneity. The enhanced inhomogeneity near cloud boundary can be attributed to strong horizontal reflectance gradients, partial cloud effects, and enhanced multiple scattering and adjacency effects between clouds and their surroundings (Bréon & Dubrulle, 2004; Oreopoulos & Cahalan, 2005; Schäfer et al., 2017; Voors et al., 2006).

4.2. Evaluation of Radiance Spectral Calibration Methods

The processing time is generally proportional to the number of wavelengths used, meaning that utilizing more channels increases computational time. Conversely, reducing the number of wavelength channels decreases processing time but may increase calibration error. Therefore, it is necessary to determine an optimal balance between efficiency and accuracy in radiance spectral calibration. For this purpose, three different approaches were tested for radiance wavelength calibration: (a) using the entire spectral window, (b) using small windows for different spectral regions, and (c) using the entire spectral range, but with relatively sparse spectral sampling. Table 4 lists the wavelength channels used in these approaches.

After classifying pixels within the same cross-track but different mirror steps as homogeneous or inhomogeneous, further analysis can be performed on wavelength shift caused by radiance spectral calibration. To quantitatively assess the difference between using the entire spectrum and using 10 small spectral windows, we define the set of differences $\Delta\boldsymbol{\alpha}_i$ for each small window with different mirror steps (No. 1–131), as follows:

$$\Delta\alpha_i = |\Delta\lambda_{\mathrm{sw}_i} - \Delta\lambda_{\mathrm{entire}}(\mathrm{sw}_i)|, i = 1, \cdots, 10, \tag{25}$$

$$\Delta\boldsymbol{\alpha}_i = \left\{\Delta\alpha_i^1, \cdots, \Delta\alpha_i^{N_{\mathrm{step}}}\right\}, i = 1, \cdots, 10, \tag{26}$$

where $\Delta\lambda_{\mathrm{sw}_i}$ represents the constant wavelength shift within the small spectral window sw_i, while $\Delta\lambda_{\mathrm{entire}}(\mathrm{sw}_i)$ denotes the wavelength shift at the center wavelength of sw_i, derived using the first-order Chebyshev-polynomial fitting within the entire spectrum. In addition, N_{step} represents the number of mirror steps within one granule, and $\Delta\boldsymbol{\alpha}_i$ describes the variation of wavelength shift errors across different mirror steps within a given small spectral window.

Figure 10 compares the wavelength shift across the UV spectral range using two approaches: (a) fitting the entire spectrum with the first-order Chebyshev polynomials, and (b) using 10 small spectral windows, each fitted with one coefficient. For the spectral tests at different intervals in approach (c), at least 250 wavelengths (with an interval of 4) are required to achieve a 1% relative error difference compared to using the entire spectrum; therefore, these results are not shown here. In this comparison, the entire-spectrum approach (a), which explicitly accounts for the wavelength dependence of the shift, is regarded as the benchmark reference. In contrast, approach (b), which does not model the wavelength dependency but uses independent fits in each small window, thus providing a simplified representation. Despite this simplification, the results from the small windows show excellent agreement with the reference values over most narrow bands, indicating that both methods produce consistent results under typical conditions.

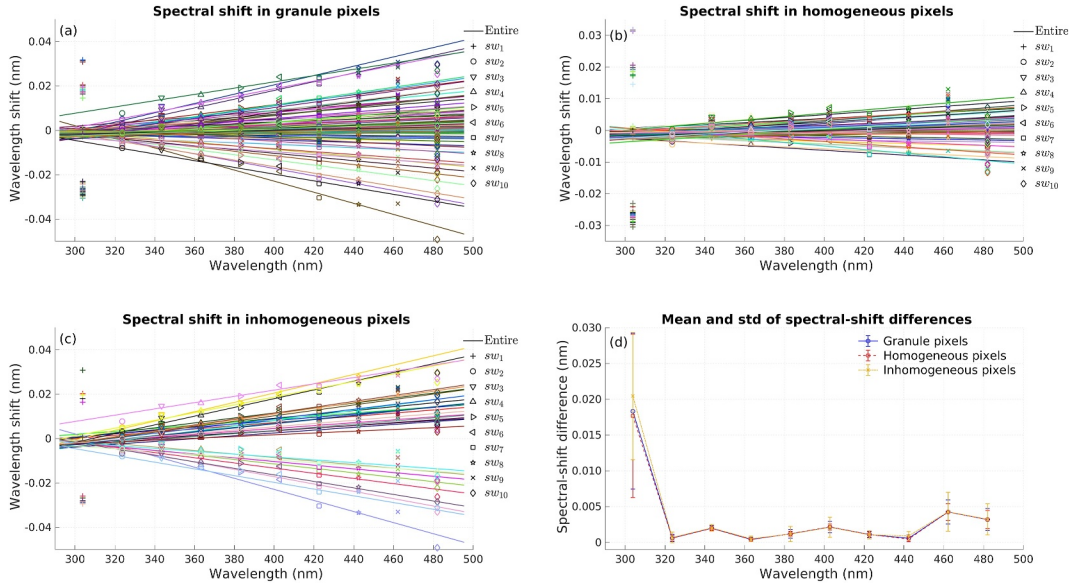

Figure 10. Comparison of wavelength shifts retrieved with the full UV spectrum (solid lines, two-term Chebyshev fit $n_p = 2$) and with 10 20 nm-wide sub-windows (symbols, single-term fits $n_p = 1, \mathrm{sw}_1 - \mathrm{sw}_{10}$) at cross-track position with xtrack = 500. Each color represents one of the 131 mirror-step pixels in the granules and is used consistently in panels (a–c). (a) Wavelength shift for all pixels. (b) Homogenous pixels only. (c) Inhomogeneous pixels only. (d) Mean absolute difference and its standard deviation between the full-spectrum and sub-windows solutions, plotted separately for all, homogenous, and inhomogeneous samples; error bars indicate one standard deviation.

In Figures 10a–10c, the solid lines represent the first-order Chebyshev-polynomial fit applied to the entire UV spectrum, while the various symbols represent zero-order (constant) fits derived from 10 individual 20 nm-wide spectral sub-windows. Each color marks a mirror-step pixel, so the same color tracks the same pixel in panels (a–c). Panel (a) shows all 131 mirror-step pixels at a cross-track position, with the wavelength shift curves derived from the first-order Chebyshev-polynomial fit changing linearly from approximately ±0.01 nm at 323.6 nm to about ±0.03 nm at 482.0 nm. Nine of the ten sub-window results are very close to these solid lines, matching in both size and slope; the only notable exception is the shortest-wavelength window, sw_1 (centered at 303.8 nm), whose wider scatter reflects a lower signal-to-noise ratio and larger radiance variations at the edge of the UV region. Restricting the data to a homogeneous set of pixels (panel b) tightens the spread, while a inhomogeneous set of pixels (panel c) widens it. Even so, most of the symbol points remain within ±0.03 nm of the full-spectrum curve, and overall trend of the spectral range is the same: either tightening or widening. In addition, both methods show significant spectral dependence in the radiance wavelength calibration, and this dependence is more pronounced under inhomogeneous conditions.

Figure 10d summarizes the comparison results by plotting the mean absolute shift difference $\overline{\Delta\alpha_i}$ for each small window and its standard deviation across all pixels. For homogeneous pixels, nine windows have $\overline{\Delta\alpha_i}$ below 0.01 nm, with corresponding standard deviation ($\sigma_{\Delta\alpha_i}$) below 0.005 nm, indicating that the small-window method is sufficiently accurate. In inhomogeneous scenes, the standard deviations roughly double, but the mean remains almost unchanged, meaning that scene inhomogeneity primarily introduces random noise rather than bias. Only sw_1 shows a larger offset ($\overline{\Delta\alpha_i} \approx 0.02$ nm, $\sigma_{\Delta\alpha_i} \approx 0.03$ nm), again pointing the limitations of short-wavelength edges. Overall, using a carefully chosen small window (100 channels, $n_p = 1$) can match the full-spectrum solution by a first-order Chebyshev-polynomial fitting (1,008 channels) within the error budget requirement (see Section 4.3), while reducing computation time by approximately tenfold. However, it cannot account for the spectral dependence in the radiance wavelength calibration.

4.3. Small Spectral Window Selection

To optimize the balance between efficiency and accuracy in radiance spectral calibration, a comprehensive wavelength channel test showed that using a small window containing 100 wavelength channels is a superior

10.1029/2025EA004637

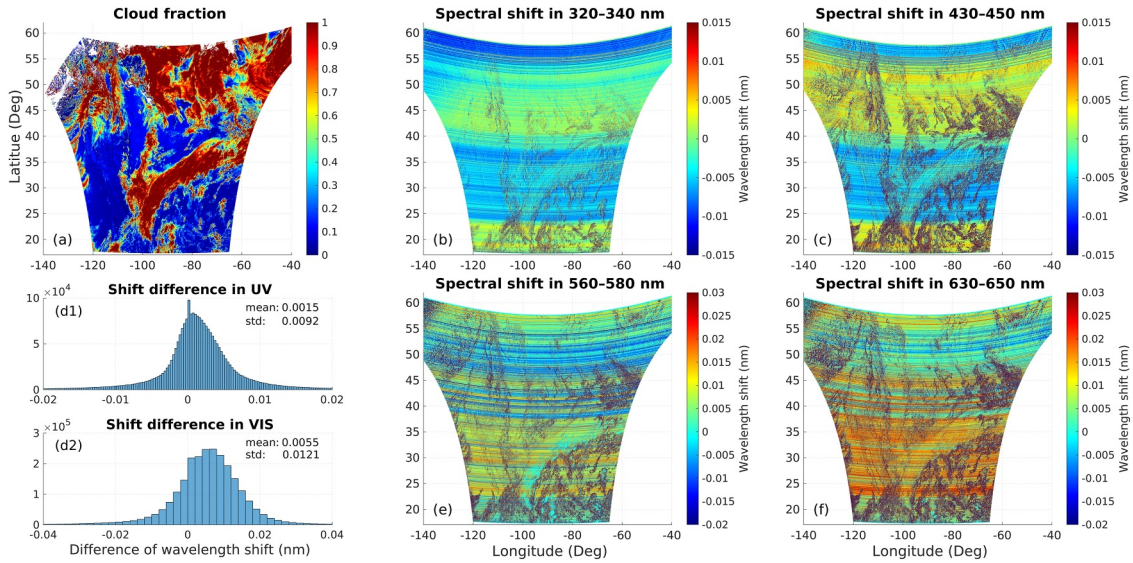

Figure 11. Comparison of radiance wavelength shifts in the selected small spectral window for a single scan in UV and VIS, along with differences between small windows and cloud fraction. (a) Cloud fraction, (b) wavelength shift in 320–340 nm in UV, (c) wavelength shift in 430–450 nm in UV, (d) histogram of the differences between small spectral windows, (e) wavelength shift in 560–580 nm in VIS, (f) wavelength shift in 630–650 nm in VIS.

solution compared to using the entire spectrum or selecting channels with varying intervals. However, the saturation probability of the small spectral window needs to be considered, as pixel saturation can lead to calibration failure. Taking into account the saturation probability (Chong et al., 2026), we select small spectral windows of 320–340 nm in the UV and 630–650 nm in the VIS for operational radiance wavelength calibration, and use the wavelength shift within these windows as representative wavelength shifts in the UV and VIS regions.

Figure 11 compares the radiance wavelength shift within the selected small spectral windows with the lowest saturation in the UV and VIS bands, as well as the difference between these small windows. In the UV spectral range, the radiance in the 320–340 nm is significantly lower than that in the 430–450 nm due to stronger ozone absorption. This results in higher scene spatial uniformity in the 320–340 nm range, thus reducing the wavelength shift patterns caused by scene inhomogeneities. This observation is consistent with the cloud boundary patterns identified in the cloud fraction data. In the VIS region, due to the similar magnitudes of radiance, the wavelength shift patterns in the 560–580 nm and 630–650 nm are similar. However, there are some differences in homogeneity at different cross-track positions. Based on histogram analysis of the differences in small spectral windows, the mean error in the UV and VIS are 0.0015 and 0.0055 nm, respectively, with standard deviations of 0.0092 and 0.0121 nm. These results can also be considered as the uncertainty introduced by using small spectral windows for radiance wavelength shift estimation.

To quantitatively compare the different small spectral windows, Table 5 lists the mean and standard deviation of the differences between a complete TEMPO scan and homogenous and inhomogeneous pixels. For homogeneous pixels, the mean difference is 0.0015 nm (UV) and 0.0059 nm (VIS), with standard deviation of 0.0043 nm (UV) and 0.0094 nm (VIS), respectively. For inhomogeneous pixels, the mean differences are 0.0017 nm (UV) and −0.0014 nm (VIS), with standard deviation of 0.0212 nm (UV) and 0.0349 nm (VIS), respectively. These results indicate that the standard deviation of the differences in inhomogeneous pixels is significantly larger than that in homogeneous ones. Additionally, the standard deviation in the VIS band is much larger than that in the UV, emphasizing the complexity of wavelength shift variations in the VIS region. This is mainly due to the presence of a distinct etalon structure at wavelengths above 630 nm, as shown in Figures 3 and 4.

Table 5
Mean and Standard Deviation (std) of the Difference Between Small Spectral Windows in the UV and VIS Bands for Homogeneous and Inhomogeneous Pixels

	UV		VIS	
Pixel type	Mean (nm)	std (nm)	Mean (nm)	std (nm)
Entire scan	0.0015	0.0092	0.0055	0.0121
Homogeneity	0.0015	0.0043	0.0059	0.0094
Inhomogeneity	0.0017	0.0212	−0.0014	0.0349

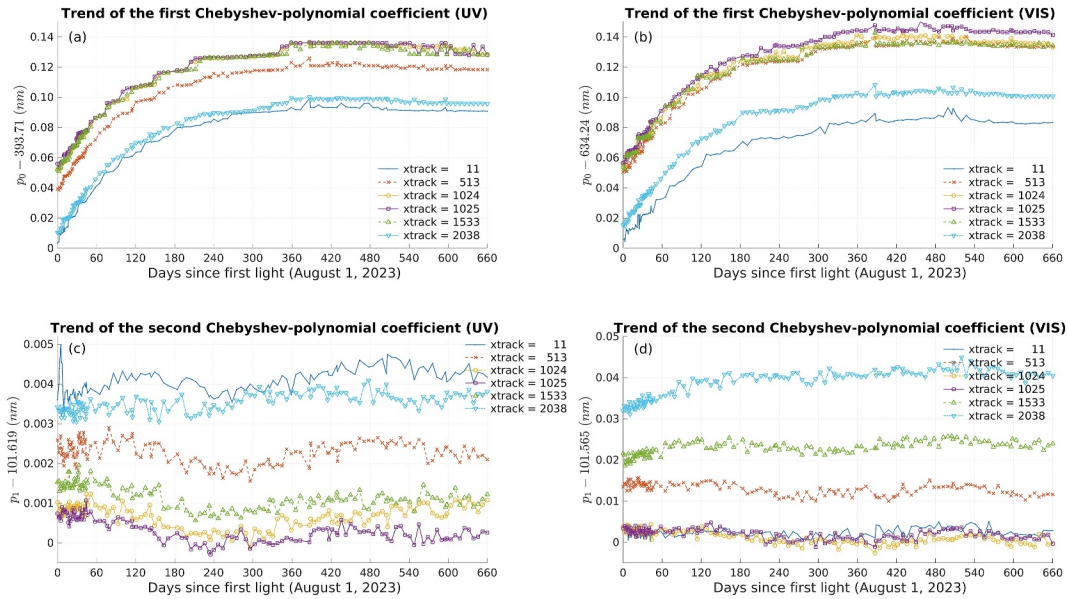

Figure 12. Time-series trends of the first two Chebyshev polynomial coefficients (p_0, p_1) in the solar irradiance spectral calibration for a representative cross-track, spanning from the first light over 22 months in UV (left panel, $n_p = 2$) and VIS (right panel, $n_p = 3$). The vertical axis has been adjusted by subtracting a fixed value to better visualize coefficient differences. (a): p_0 trend in UV, (b): p_0 trend in VIS, (c) p_1 trend in UV, (d) p_1 trend in VIS. The clustering of data points in the first ∼45 days reflects the commissioning phase, during which solar irradiance measurements were taken more frequently. During nominal operations starting in October 2023, solar observations have been conducted weekly using the working diffuser.

5. Trending Analysis

5.1. Wavelength Shift Trending for Irradiance

For irradiance wavelength calibration using absolute spectral calibration, first-order Chebyshev-polynomial fitting ($n_p = 2$) is used for the UV, and second-order fitting ($n_p = 3$) is used for the VIS. For $n_p = 2$, Equation 5 simplifies to a linear relationship between the spectral pixel index and the wavelength:

$$\lambda(i) = p_0 + \frac{2 * i - N + 1}{N - 1} p_1, (i = 1, \cdots, 1028), \tag{27}$$

where the numeric range is:

$$\lambda(i) \in \left[p_0 - p_1, p_0 + p_1\right], (i = 1, \cdots, 1028). \tag{28}$$

Physically, p_0 represents the center wavelength of the spectral range, and p_1 defines the extended range extension on both sides.

Figure 12 illustrates the time-trend assessment of the first two Chebyshev-polynomial coefficients (p_0, p_1) of a typical cross-track over 22 months following the first light in both the UV and VIS regions. The vertical axis is offset by a fixed value to better illustrate the coefficient differences. As shown, p_0 gradually increases over time in both spectral regions, while p_1 remains relatively stable. This suggests a systematic shift in the wavelength grid, but the magnitude of the shift remains consistent across different spectral pixels, with minimal spectral variability.

Figure 13 further illustrates the wavelength shift trends obtained from solar irradiance wavelength calibration relative to the first light. The increasing trend of p_0, combined with the relatively stable p_1, leads to a net wavelength shift over time. Specifically, the wavelength shifts at 330 and 440 nm in the UV, as well as at 640 and 710 nm in the VIS, both show a gradually increasing trend, highlighting the initial spectral drift of the spectral calibration. However, since around July 2024, the rate of change in wavelength shift has slowed down and become relatively stable.

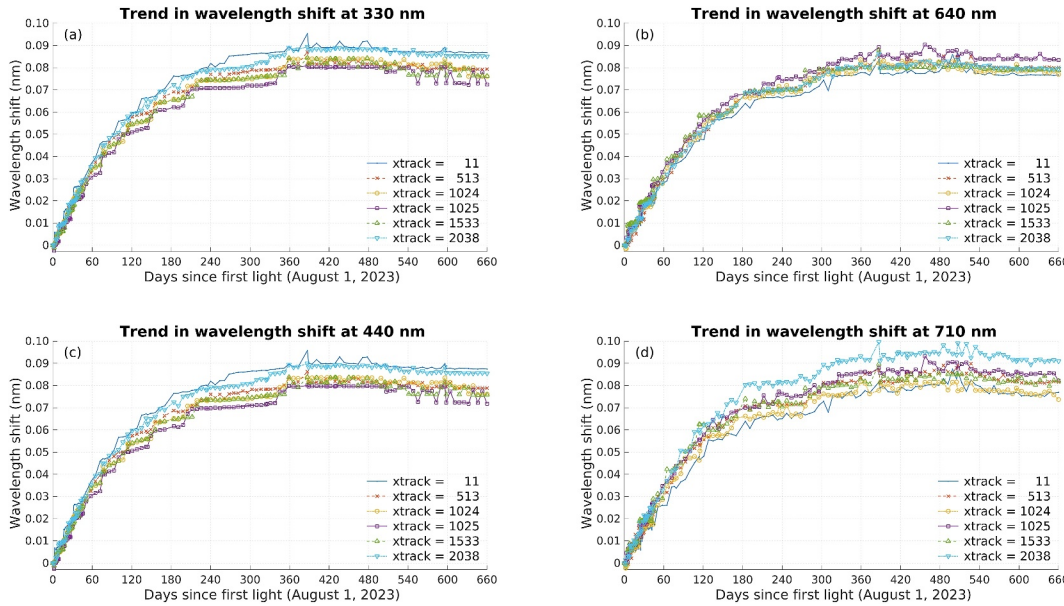

Figure 13. Time-series trending of wavelength shifts (changes) in solar irradiance spectral calibration relative to the first light, for a typical cross-track and specific wavelength in UV (left panel, $n_p = 2$) and VIS (right panel, $n_p = 3$) (a, c) Wavelength shift at 330 and 440 nm (b, d) wavelength shift at 640 and 710 nm. Data density variations are consistent with Figure 12, due to differing solar observation frequencies during commissioning and nominal operations.

5.2. Slit Function (Shape, hw1e) Parameters Trending

Figure 14 displays the time-series variation trends of the super-Gaussian slit function parameters (shape and hw1e) within small spectral windows from the first light onward. The prelaunch values are denoted by the x-tick "−1." A total of nine small windows in UV and seven in VIS were analyzed.

In the UV region, except for 425 nm, the shape parameter of most small windows generally increases compared to the prelaunch. Notably, the shape value of the 297.8 nm, 310 nm, and 320 nm windows increases significantly by 0.4–0.6. However, after the first-light observation, the shape parameter of most spectral windows gradually decreases, except for 330 and 425 nm. While the 330 nm window remains relatively stable after a gradual increase for about 90 days, the 425 nm window shows an increase in shape value over the first roughly 240 days. For the hw1e parameter in UV, only slight fluctuations (±0.005) are observed compared with the prelaunch, but overall, these indicate that no significant changes have occurred since the first light.

In the VIS region, except for two small edge windows at 705 and 736 nm, the slit-function parameters remain relatively stable compared to prelaunch. Within these two edge windows, the values of shape and hw1e show relatively large variations. These results indicate that the slit function parameters retrieved from the small spectral windows can be effectively used for long-term trend monitoring, providing insights into TEMPO's stability and spectral consistency over extended operational periods.

6. Summary and Conclusion

This study focuses on the spectral calibration, a crucial component of the TEMPO Version 3 Level 0–1 data processing system, which plays a vital role in ensuring the quality of Level 1b data. The spectral calibration methods employed by Version 3 Level 0–1 processor are systematically introduced, covering their theoretical framework and on-orbit implementation. Specifically, the operational wavelength calibration procedures for Level 1 solar irradiance and Earth-view radiance spectra are summarized, and strategies for maintaining long-term stability of measurement performance are described. Furthermore, the offline configuration and parameter selection used to derive the on-orbit slit function are detailed, which is essential for accurately characterizing the instrument's spectral response. These elements collectively ensure the reliability and traceability of wavelength calibration for TEMPO hyperspectral observations.

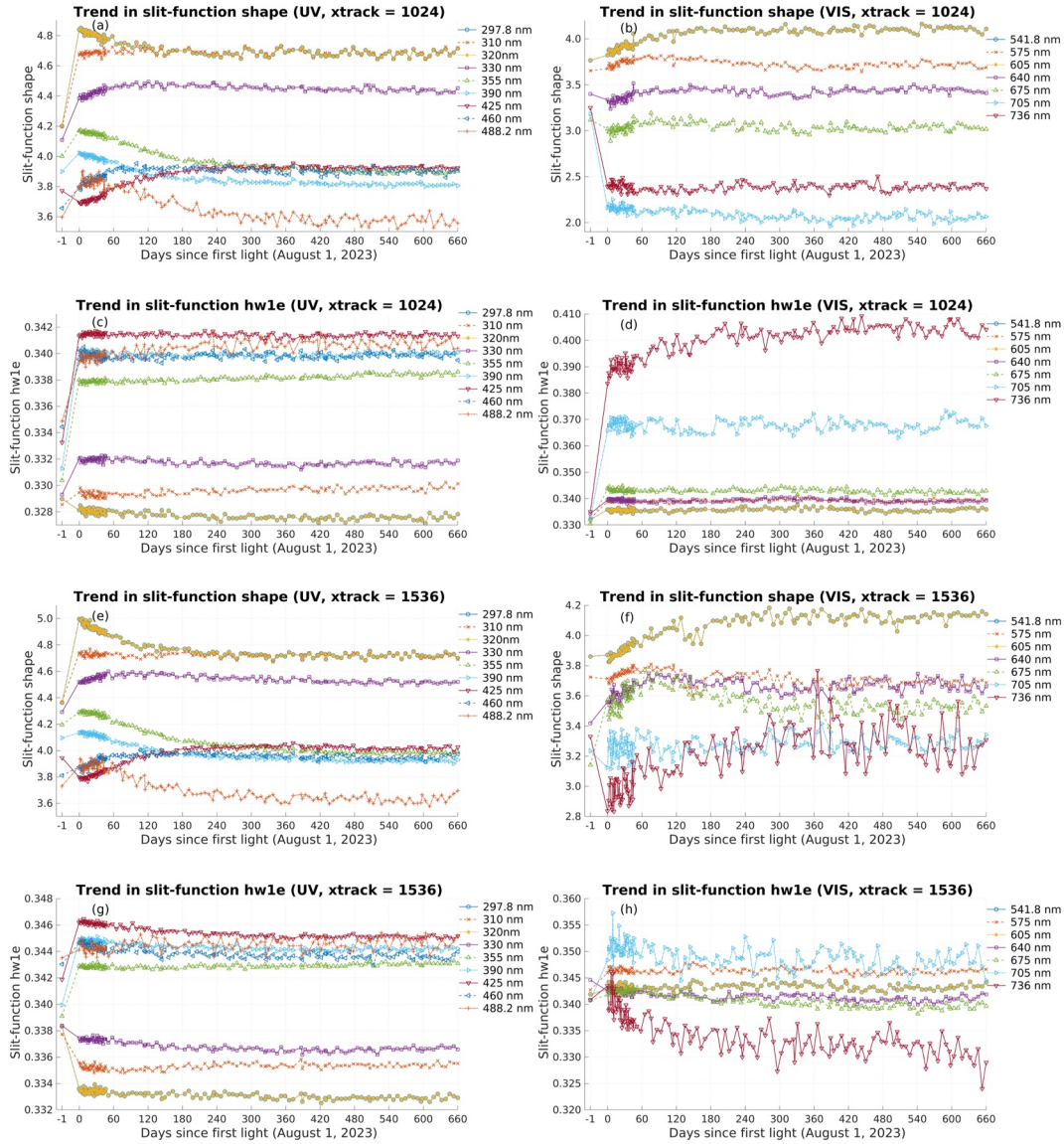

Figure 14. Time-series trends of super-Gaussian slit function parameters (shape, hw1e) from first light, measured in small spectral window in UV (left panel) and VIS (right panel). The x-tick "−1" represents the prelaunch result. The data density variations are consistent with those in Figure 12, reflecting the higher observation frequency during commissioning compared to nominal operations.

To perform irradiance spectral calibration, we analyzed solar irradiance data from TEMPO since its first light. The spectral fitting accuracy for irradiance calibration was evaluated relative to different reference solar spectra (e.g., SAO2010 and TSIS-1 HSRS). Preliminary fitting results showed lower fitting errors when using the TSIS-1 HSRS as the reference spectrum, therefore TSIS-1 HSRS was chosen as the final reference spectrum. We investigated the effect of Chebyshev polynomials order on wavelength shift and found that higher-order Chebyshev polynomials lead to spurious oscillations (i.e., Runge Phenomenon). Therefore, in operational processing, we used first-order and second-order Chebyshev polynomial to fit the UV and VIS, respectively, as the mathematical functions for spectral calibration. We extracted the offline key parameters of the super-Gaussian slit function from several small spectral windows and smoothed them using interpolations, employ cubic Hermite interpolation for both the UV and VIS. Due to the low retrievability, the slit function asymmetry factor (e.g., hw1e asymmetry a_w) was also set to zero to minimize noise. It should be noted that the current analysis represents only a preliminary offline study; future research will incorporate more comprehensive parameter coupling and slit function normalization to ensure complete physical consistency across wavelength and spatial dimensions.

For Earth-view radiance wavelength calibration, we primarily investigated the effects of scene inhomogeneity and optimal spectral calibration. A threshold-based method was tested to classify pixels into homogeneous and inhomogeneous categories. Inhomogeneous pixels is aligned with cloud boundaries, providing useful information for subsequent inhomogeneity. In operational processing, to avoid the probability of saturation, we selected two small spectral windows, 320–340 nm (UV) and 630–650 nm (VIS), for radiance spectral calibration. Each window contains 100 channels, and the wavelength shift within these two windows was used as the representative shifts for the UV and VIS, respectively. Uncertainty analysis using these small spectral windows shows that the mean error for UV is about 0.002 nm, and for VIS is 0.006 nm, with standard deviations of 0.009 and 0.012 nm, respectively. Furthermore, the standard deviation of the wavelength shift differences for inhomogeneous pixels is significantly larger than that for homogeneous pixels. While using a small spectral window can speed up the online processing, it cannot account for the spectral dependence in the radiance wavelength calibration, especially for inhomogeneous pixels.

In addition, to monitor long-term performance of TEMPO solar irradiance data, we performed trend analysis on wavelength shift and offline slit function parameters over approximately 22 months after the first light. Analysis of one-order Chebyshev polynomial coefficients fitted to the UV showed that the spectral center point (p_0) gradually increased over time, leading to a new wavelength shift, while the spectral range (p_1) remains stable. Meanwhile, the shape and width of the slit function within small spectral windows were tracked in UV and VIS. The shape in UV generally decreased after the first light, except for stabilization or slight increases at 330 and 425 nm. The shape and width in most VIS channels were relatively stable, except for the spectral edges at 705 and 736 nm. Significant deviations occur at these two spectral edges, partly because the known etalon structure is not corrected in TEMPO Version 3 Level 1b solar irradiance data.

The results of this study suggest the long-term robustness of the TEMPO spectral calibration approach, further enhancing the reliability of on-orbit calibration in long-term atmospheric monitoring. As TEMPO continues to provide high-resolution, near-real-time observations over North America, the spectral calibration methodologies described in this contribution are essential to maintain long-term data quality for atmospheric studies and various applications.

Conflict of Interest

The authors declare no conflicts of interest relevant to this study.

Data Availability Statement

The Version 3 TEMPO Level 1 products are publicly available at the NASA ASDC via the link: https://asdc.larc.nasa.gov/project/TEMPO. The solar reference spectrum published by the SAO in 2010 (SAO2010) is available at: https://lweb.cfa.harvard.edu/atmosphere/links/sao2010.solref.converted. Version 2 of the Total and Spectral Solar Irradiance Sensor-1 (TSIS-1) HSRS is available at: https://lasp.colorado.edu/lisird/data/tsis1_hsrs_p1nm.

Acknowledgments
TEMPO is NASA's first Earth Venture Instrument (EVI-1) mission, led by the Smithsonian Astrophysical Observatory (SAO), with project management provided by NASA's Langley Research Center (LaRC) and instrument development by Ball Aerospace (now BAE Systems). This study was supported by NASA TEMPO contract (NNL13AA09C) and the NASA SNWG TEMPO Near Real Time contract (80MSFC24CA004), and SAO's subaward S03939-01 to NASA grant 80NSSC22K1047. The Atmospheric Science Data Center (ASDC) at NASA LaRC is responsible for the archiving and distribution of TEMPO data products. J. Wang's contribution is made possible by in-kind support through Lichtenberger Family Chair professor in Chemical Engineering in the University of Iowa.

References

Bak, J., Liu, X., Kim, J. H., Haffner, D. P., Chance, K., Yang, K., & Sun, K. (2017). Characterization and correction of OMPS nadir mapper measurements for ozone profile retrievals. *Atmospheric Measurement Techniques*, *10*(11), 4373–4388. https://doi.org/10.5194/amt-10-4373-2017

Beirle, S., Lampel, J., Lerot, C., Sihler, H., & Wagner, T. (2017). Parameterizing the instrumental spectral response function and its changes by a super-Gaussian and its derivatives. *Atmospheric Measurement Techniques*, *10*(2), 581–598. https://doi.org/10.5194/amt-10-581-2017

Beirle, S., Sihler, H., & Wagner, T. (2013). Linearisation of the effects of spectral shift and stretch in DOAS analysis. *Atmospheric Measurement Techniques*, *6*(3), 661–675. https://doi.org/10.5194/amt-6-661-2013

Bréon, F.-M., & Dubrulle, B. (2004). Horizontally oriented plates in clouds. *Journal of the Atmospheric Sciences*, *61*(23), 2888–2898. https://doi.org/10.1175/JAS-3309.1

Cai, Z., Liu, Y., Liu, X., Chance, K., Nowlan, C. R., Lang, R., et al. (2012). Characterization and correction of global ozone monitoring experiment 2 ultraviolet measurements and application to ozone profile retrievals. *Journal of Geophysical Research*, *117*(D7). https://doi.org/10.1029/2011jd017096

Caspar, C., & Chance, K. (1997). GOME wavelength calibration using solar and atmospheric spectra. In *Proceedings of the 3rd ERS Symposium on Space at the Service of Our Environment* (Vol. 2).

Chan, K. L., Wiegner, M., van Geffen, J., De Smedt, I., Alberti, C., Cheng, Z., et al. (2020). MAX-DOAS measurements of tropospheric NO2 and HCHO in Munich and the comparison to OMI and TROPOMI satellite observations. *Atmospheric Measurement Techniques*, *13*(8), 4499–4520. https://doi.org/10.5194/amt-13-4499-2020

Chance, K., & Kurucz, R. L. (2010). An improved high-resolution solar reference spectrum for earth's atmosphere measurements in the ultraviolet, visible, and near infrared. *Journal of Quantitative Spectroscopy and Radiative Transfer*, *111*(9), 1289–1295. https://doi.org/10.1016/j.jqsrt.2010.01.036

Chance, K., Palmer, P. I., Spurr, R. J., Martin, R. V., Kurosu, T. P., & Jacob, D. J. (2000). Satellite observations of formaldehyde over North America from GOME. *Geophysical Research Letters*, *27*(21), 3461–3464. https://doi.org/10.1029/2000gl011857

Chan Miller, C., Roche, S., Wilzewski, J. S., Liu, X., Chance, K., Souri, A. H., et al. (2024). Methane retrieval from MethaneAIR using the CO2 proxy approach: A demonstration for the upcoming MethaneSAT mission. *Atmospheric Measurement Techniques*, *17*(18), 5429–5454. https://doi.org/10.5194/amt-17-5429-2024

Chong, H., Liu, X., Houck, J. C., Flittner, D. E., Carr, J. L., Hou, W., & Carpenter, L. (2026). Algorithm theoretical basis for version 3 TEMPO level 0-1 processor. *Earth and Space Science*, *13*, e2025EA004516. https://doi.org/10.1029/2025EA004516

Cleveland, W. S., & Devlin, S. J. (1988). Locally weighted regression: An approach to regression analysis by local fitting. *Journal of the American Statistical Association*, *83*(403), 596–610. https://doi.org/10.1080/01621459.1988.10478639

Coddington, O. M., Richard, E. C., Harber, D., Pilewskie, P., Woods, T. N., Snow, M., et al. (2023). Version 2 of the TSIS-1 hybrid solar reference spectrum and extension to the full spectrum. *Earth and Space Science*, *10*(3), e2022EA002637. https://doi.org/10.1029/2022EA002637

Conway, E. K., Souri, A. H., Benmergui, J., Sun, K., Liu, X., Staebell, C., et al. (2024). Level0 to Level1B processor for MethaneAIR. *Atmospheric Measurement Techniques*, *17*(4), 1347–1362. https://doi.org/10.5194/amt-17-1347-2024

Courrèges-Lacoste, G. B., Ahlers, B., Guldimann, B., Short, A., Veihelmann, B., & Stark, H. (2011). *The Sentinel-4/UVN instrument on-board MTG-S, paper presented at Proceedings of 2011 EUMETSAT Meteorological Satellite Conference*. EUMETSAT.

Dirksen, R., Dobber, M., Voors, R., & Levelt, P. (2006). Prelaunch characterization of the ozone monitoring instrument transfer function in the spectral domain. *Applied Optics*, *45*(17), 3972–3981. https://doi.org/10.1364/AO.45.003972

Gonzalez Abad, G., Souri, A. H., Bak, J., Chance, K., Flynn, L. E., Krotkov, N. A., et al. (2019). Five decades observing Earth's atmospheric trace gases using ultraviolet and visible backscatter solar radiation from space. *Journal of Quantitative Spectroscopy and Radiative Transfer*, *238*, 106478. https://doi.org/10.1016/j.jqsrt.2019.04.030

Hadjimitsis, D. G., Themistocleous, K., Michaelides, S., Papadavid, G., Ahn, M.-H., Kang, M., et al. (2015). A sensitivity study for the calibration of hyperspectral spectrometer on board the geostationary multipurpose satellite of Korea (Vol. *9535*). https://doi.org/10.1117/12.2192534

Hamidouche, M., & Lichtenberg, G. n. (2018). In-Flight retrieval of SCIAMACHY instrument spectral response function. *Remote Sensing*, *10*(3), 401. https://doi.org/10.3390/rs10030401

Kang, M., Ahn, M.-H., Liu, X., Jeong, U., & Kim, J. (2020). Spectral calibration algorithm for the geostationary environment monitoring spectrometer (GEMS). *Remote Sensing*, *12*(17), 2846. https://doi.org/10.3390/rs12172846

Kleipool, Q., Ludewig, A., Babić, L., Bartstra, R., Braak, R., Dierssen, W., et al. (2018). Pre-launch calibration results of the TROPOMI payload on-board the Sentinel-5 precursor satellite. *Atmospheric Measurement Techniques*, *11*(12), 6439–6479. https://doi.org/10.5194/amt-11-6439-2018

Liu, C., Liu, X., Kowalewski, M. G., Janz, S. J., González Abad, G., Pickering, K. E., et al. (2015a). Analysis of ACAM data for trace gas retrievals during the 2011 DISCOVER-AQ campaign. *Journal of Spectroscopy*, *2015*, 1–7. https://doi.org/10.1155/2015/827160

Liu, C., Liu, X., Kowalewski, M. G., Janz, S. J., González Abad, G., Pickering, K. E., et al. (2015b). Characterization and verification of ACAM slit functions for trace-gas retrievals during the 2011 DISCOVER-AQ flight campaign. *Atmospheric Measurement Techniques*, *8*(2), 751–759. https://doi.org/10.5194/amt-8-751-2015

Liu, X., Bhartia, P. K., Chance, K., Froidevaux, L., Spurr, R. J. D., & Kurosu, T. P. (2010). Validation of ozone monitoring instrument (OMI) ozone profiles and stratospheric ozone columns with microwave limb sounder (MLS) measurements. *Atmospheric Chemistry and Physics*, *10*(5), 2539–2549. https://doi.org/10.5194/acp-10-2539-2010

Liu, X., Chance, K., Sioris, C. E., & Kurosu, T. P. (2007). Impact of using different ozone cross sections on ozone profile retrievals from global ozone monitoring experiment (GOME) ultraviolet measurements. *Atmospheric Chemistry and Physics*, *7*(13), 3571–3578. https://doi.org/10.5194/acp-7-3571-2007

Liu, X., Chance, K., Sioris, C. E., Spurr, R. J. D., Kurosu, T. P., Martin, R. V., & Newchurch, M. J. (2005). Ozone profile and tropospheric ozone retrievals from the global ozone monitoring experiment: Algorithm description and validation. *Journal of Geophysical Research*, *110*(D20). https://doi.org/10.1029/2005jd006240

Ludewig, A., Kleipool, Q., Bartstra, R., Landzaat, R., Leloux, J., Loots, E., et al. (2020). In-flight calibration results of the TROPOMI payload on board the Sentinel-5 precursor satellite. *Atmospheric Measurement Techniques*, *13*(7), 3561–3580. https://doi.org/10.5194/amt-13-3561-2020

Markwardt, C. (2012). MPFIT: Robust non-linear least squares curve fitting, Astrophysics source code library, ascl: 1208 (p. 1019).

MathWorks. (2024). *MATLAB, version R2024a*. The MathWorks, Inc.

Munro, R., Lang, R., Klaes, D., Poli, G., Retscher, C., Lindstrot, R., et al. (2016). The GOME-2 instrument on the Metop series of satellites: Instrument design, calibration, and level 1 data processing – An overview. *Atmospheric Measurement Techniques*, *9*(3), 1279–1301. https://doi.org/10.5194/amt-9-1279-2016

Noël, S., Bramstedt, K., Bovensmann, H., Gerilowski, K., Burrows, J. P., Standfuss, C., et al. (2012). Quantification and mitigation of the impact of scene inhomogeneity on Sentinel-4 UVN UV-VIS retrievals. *Atmospheric Measurement Techniques*, *5*(6), 1319–1331. https://doi.org/10.5194/amt-5-1319-2012

Nowlan, C. R., Liu, X., Janz, S. J., Kowalewski, M. G., Chance, K., Follette-Cook, M. B., et al. (2018). Nitrogen dioxide and formaldehyde measurements from the GEOstationary coastal and air pollution events (GEO-CAPE) airborne simulator over Houston, Texas. *Atmospheric Measurement Techniques*, *11*(11), 5941–5964. https://doi.org/10.5194/amt-11-5941-2018

Nowlan, C. R., Liu, X., Leitch, J. W., Chance, K., González Abad, G., Liu, C., et al. (2016). Nitrogen dioxide observations from the geostationary trace gas and aerosol sensor optimization (GeoTASO) airborne instrument: Retrieval algorithm and measurements during DISCOVER-AQ Texas 2013. *Atmospheric Measurement Techniques*, *9*(6), 2647–2668. https://doi.org/10.5194/amt-9-2647-2016

Oreopoulos, L., & Cahalan, R. F. (2005). Cloud inhomogeneity from MODIS. *Journal of Climate*, *18*(23), 5110–5124. https://doi.org/10.1175/JCLI3591.1

Schäfer, M., Bierwirth, E., Ehrlich, A., Jäkel, E., Werner, F., & Wendisch, M. (2017). Directional, horizontal inhomogeneities of cloud optical thickness fields retrieved from ground-based and airbornespectral imaging. *Atmospheric Chemistry and Physics*, *17*(3), 2359–2372. https://doi.org/10.5194/acp-17-2359-2017

Seftor, C. J., Jaross, G., Kowitt, M., Haken, M., Li, J., & Flynn, L. E. (2014). Postlaunch performance of the Suomi National Polar-orbiting partnership ozone mapping and profiler suite (OMPS) nadir sensors. *Journal of Geophysical Research: Atmospheres*, *119*(7), 4413–4428. https://doi.org/10.1002/2013JD020472

Sihler, H., Lübcke, P., Lang, R., Beirle, S., de Graaf, M., Hörmann, C., et al. (2016). In-operation field of view retrieval (IFR) for satellite and ground-based DOAS-Type instruments applying coincident high-resolution imager data. *Atmospheric Measurement Techniques Discussions*. https://doi.org/10.5194/amt-2016-218

Sun, K., Liu, X., Huang, G., González Abad, G., Cai, Z., Chance, K., & Yang, K. (2017). Deriving the slit functions from OMI solar observations and its implications for ozone-profile retrieval. *Atmospheric Measurement Techniques*, *10*(10), 3677–3695. https://doi.org/10.5194/amt-10-3677-2017

Sun, K., Liu, X., Nowlan, C. R., Cai, Z., Chance, K., Frankenberg, C., et al. (2017). Characterization of the OCO-2 instrument line shape functions using on-orbit solar measurements. *Atmospheric Measurement Techniques*, *10*(3), 939–953. https://doi.org/10.5194/amt-10-939-2017

van den Oord, G. H. J., Rozemeijer, N., Schenkelaars, V., Levelt, P., Dobber, M., Voors, R., et al. (2006). OMI level 0 to 1b processing and operational aspects. *IEEE Transactions on Geoscience and Remote Sensing*, *44*(5), 1380–1397. https://doi.org/10.1109/tgrs.2006.872935

van Geffen, J. H. G. M. (2004). Wavelength calibration of spectral measured by the global ozone monitoring experiment: Variations along orbits and in time. *Applied Optics*, *43*(3), 695–706. https://doi.org/10.1364/ao.43.000695

van Geffen, J. H. G. M., & van Oss, R. F. (2003). Wavelength calibration of spectra measured by the global ozone monitoring experiment by use of a high-resolution reference spectrum. *Applied Optics*, *42*(15), 2739–2753. https://doi.org/10.1364/ao.42.002739

Voors, R., Dobber, M., Dirksen, R., & Levelt, P. (2006). Method of calibration to correct for cloud-induced wavelength shifts in the Aura satellite's ozone monitoring instrument. *Applied Optics*, *45*(15), 3652–3658. https://doi.org/10.1364/AO.45.003652

Wang, H., Nowlan, C. R., González Abad, G., Chong, H., Hou, W., Houck, J. C., et al. (2025). Algorithm theoretical basis for version 3 TEMPO O2-O2 cloud product. *Earth and Space Science*, *12*(2), e2024EA004165. https://doi.org/10.1029/2024EA004165

Zoogman, P., Liu, X., Suleiman, R., Pennington, W., Flittner, D., Al-Saadi, J., et al. (2017). Tropospheric emissions: Monitoring of pollution (TEMPO). *Journal of Quantitative Spectroscopy and Radiative Transfer*, *186*, 17–39. https://doi.org/10.1016/j.jqsrt.2016.05.008